A 4DVAR System for the Navy Coastal Ocean Model. Part I: System Description and Assimilation of Synthetic Observations in Monterey Bay*

Hans Ngodock and Matthew Carrier

Naval Research Laboratory, Stennis Space Center, Mississippi

(Manuscript received 9 July 2013, in final form 27 December 2013)

ABSTRACT

A 4D variational data assimilation system was developed for assimilating ocean observations with the Navy Coastal Ocean Model. It is described in this paper, along with initial assimilation experiments in Monterey Bay using synthetic observations. The assimilation system is tested in a series of twin data experiments to assess its ability to fit assimilated and independent observations by controlling the initial conditions and/or the external forcing while assimilating surface and/or subsurface observations. In all strong and weak constraint experiments, the minimization of the cost function is done with both the gradient descent method (in the control space) and the representer method (observation space). The accuracy of the forecasts following the analysis and the relevance of the retrieved forcing correction in the case of weak constraints are evaluated. It is shown that the assimilation system generally fits the assimilated and nonassimilated observations well in all experiments, yielding lower forecast errors.

1. Introduction

This paper describes the development of a four-dimensional variational data assimilation (4DVAR) system based on the representer method for the Navy Coastal Ocean Model (NCOM). NCOM is an operational ocean model (primarily at the Naval Oceanographic Office) that has been validated (Martin 2000; Barron et al. 2006), with several references in the literature. It is a free-surface general circulation model (GCM) based on the primitive equations and employs the hydrostatic, Boussinesq, and incompressible approximations. It has been used in global- and basin-scale circulation applications (Barron et al. 2003, 2004; Kara et al. 2006); in coastal applications, for example, to model the upwelling and relaxation events in Monterey Bay (Shulman et al. 2007); and river discharge (Morey et al. 2003) and river plume modeling (Liu et al. 2009); and in modeling air–sea interactions through coupling with atmospheric models (Pullen et al. 2006, 2007).

Other applications include particle transport (Haza et al. 2007; Schroeder et al. 2011), the tracking of oil spills in Australia (Brushett et al. 2011) and in the Gulf of Mexico (Cheng et al. 2011), the tracking of eddies and filaments (Burrage et al. 2009), the study of bottom Ekman tidal flows (Book et al. 2009), and the coupling to ecosystem (Jolliff et al. 2009) and biochemical and bio-optical models (Shulman et al. 2011).

Other models of the complexity of NCOM have seen similar 4DVAR development efforts undertaken in the past decade. A 4DVAR assimilation system was developed for the Ocean Parallelisé (OPA) model (Weaver et al. 2003), for the Massachusetts Institute of Technology's (MIT) general circulation model (MITgcm; Marotzke et al. 1999) also used in the Estimation of the Circulation and Climate of the Ocean (ECCO) consortium assimilation experiments (Stammer et al. 2002), and a similar system was built for the Regional Ocean Model System (ROMS; Moore et al. 2004). Unlike the other models using fixed z levels (OPA and MITgcm) or s coordinates (ROMS), NCOM uses a hybrid vertical coordinate that combines dynamic sigma layers in the upper ocean and fixed z levels below, or a generalized vertical coordinate with dynamic sigma layers, static sigma layers, and z levels. Dynamic sigma layers evolve with the free surface and static sigma layers are prescribed a fixed-depth fraction that is kept constant throughout a given model simulation.

Report Documentation Page

1. REPORT DATE **JUN 2014**	2. REPORT TYPE	3. DATES COVERED **00-00-2014 to 00-00-2014**

4. TITLE AND SUBTITLE	5a. CONTRACT NUMBER
A 4DVAR System for the Navy Coastal Ocean Model. Part I: System Description and Assimilation of Synthetic Observations in Monterey Bay	5b. GRANT NUMBER
	5c. PROGRAM ELEMENT NUMBER
6. AUTHOR(S)	5d. PROJECT NUMBER
	5e. TASK NUMBER
	5f. WORK UNIT NUMBER

7. PERFORMING ORGANIZATION NAME(S) AND ADDRESS(ES) **Naval Research Laboratory,1 Stennis Space Ctr,Stennis Space Center,MS,39529**	8. PERFORMING ORGANIZATION REPORT NUMBER

9. SPONSORING/MONITORING AGENCY NAME(S) AND ADDRESS(ES)	10. SPONSOR/MONITOR'S ACRONYM(S)
	11. SPONSOR/MONITOR'S REPORT NUMBER(S)

12. DISTRIBUTION/AVAILABILITY STATEMENT
Approved for public release; distribution unlimited

13. SUPPLEMENTARY NOTES

14. ABSTRACT

A 4D variational data assimilation system was developed for assimilating ocean observations with the Navy Coastal Ocean Model. It is described in this paper, along with initial assimilation experiments in Monterey Bay using synthetic observations. The assimilation system is tested in a series of twin data experiments to assess its ability to fit assimilated and independent observations by controlling the initial conditions and/or the external forcing while assimilating surface and/or subsurface observations. In all strong and weak constraint experiments, the minimization of the cost function is done with both the gradient descent method (in the control space) and the representer method (observation space). The accuracy of the forecasts following the analysis and the relevance of the retrieved forcing correction in the case of weak constraints are evaluated. It is shown that the assimilation system generally fits the assimilated and nonassimilated observations well in all experiments, yielding lower forecast errors.

15. SUBJECT TERMS

16. SECURITY CLASSIFICATION OF:			17. LIMITATION OF ABSTRACT	18. NUMBER OF PAGES	19a. NAME OF RESPONSIBLE PERSON
a. REPORT **unclassified**	b. ABSTRACT **unclassified**	c. THIS PAGE **unclassified**	**Same as Report (SAR)**	**23**	

It is a common practice to test a recently developed assimilation system with identical twin experiments in which the observations are simulated by the numerical model. Twin experiments allow us to test not only the system's ability to fit the assimilated observations, but also to test the accuracy of the analysis (and its associated forecast) away from the observation locations, the adequacy of the prescribed error covariances, and the accuracy and relevance of the retrieved corrections of the initial conditions, and the external forcing in the case of weak constraint.

All of these consistency and accuracy tests are carried out in Monterey Bay. The region is chosen for the numerous field experiments that have been conducted there along with the array of moored buoys that have collected data over a long period of time The region provides an abundant dataset that will be used for evaluating and validating the assimilation system with real observations in the second part of this study, this first part consisting of the system description and twin experiments.

The 4DVAR system is implemented with the flexibility of running either strong or weak constraint assimilation experiments. The strong constraint uses the gradient descent method for minimizing the cost function. The weak constraint is based on the representer method (Bennett 1992, 2002) in which the solution to the assimilation problem is sought as the sum of a first guess and a finite linear combination of representer functions, one per datum. The computation and storage of all the representer functions is avoided by using the indirect representer method (Amodei 1995; Egbert et al. 1994; Bennett et al. 1996; Ngodock et al. 2000). The formulation of the assimilation problem allows for the inclusion of a model error term (i.e., weak constraint) at no extra computational cost to the minimization process. In this paper, an assessment will be performed of the system's ability to fit both assimilated observations, as well as the consistency of the retrieved model forcing.

There are no specific applications of 4DVAR in Monterey Bay, let alone its weak constraint formulation. Strong constraint variational assimilation (Broquet et al. 2009) has been applied to the California Current System CCS), including an application to estimate surface forcing correction (Broquet et al. 2011), using the inverse Regional Ocean Modeling System (IROMS; Di Lorenzo et al. 2007) with horizontal resolutions of 10 and 30 km. The CCS is a large area that includes Monterey Bay, although these applications did not specifically target the bay. Most of the assimilation experiments that have been carried for Monterey Bay were based on sequential methods such as 3DVAR and ensemble-based Kalman filters (Chao et al. 2009; Haley et al. 2009; Shulman et al. 2009).

A brief description of the numerical model is presented in the next section, followed by the 4DVAR system derivation and implementation in section 3. Section 4 deals with the experiments' setup and results, and concluding remarks follow in section 5.

2. The model

NCOM is described in the literature (Martin 2000; Barron et al. 2006). The model domain used for this experiment contains the Monterey Bay, California, region. This location is favorable for ocean modeling due to its strong land–sea-breeze circulation patterns, complex coastline with steep topography, and the existence of frequent local upwelling and relaxation events (Shulman et al. 2002). The domain covers 35.6°–37.49°N and 121.38°–123.2°W with a horizontal resolution of 2 km and 50 layers in the vertical. The initial conditions were obtained from downscaling the operational $\frac{1}{8}°$ resolution global NCOM (GNCOM) to an intermediate model with horizontal resolution of 6 km, and then via a 3-to-1 nesting ratio to the 2-km model. Horizontal viscosities and diffusivities are computed using either the grid-cell Reynolds number (Re) or the Smagorinsky schemes, both of which tend to decrease as resolution is increased. The grid-cell Re scheme sets the mixing coefficient K to maintain a grid-cell Re number below a specified value (e.g., if Re $= u \times \Delta x / K = 30$, then $K = u \times \Delta x / 30$). Hence, as Δx decreases, K decreases proportionally. A similar computation is performed for the Smagorinsky scheme.

Surface boundary conditions (e.g., wind stress, IR radiation flux, etc.) are provided by the Coupled Ocean–Atmosphere Mesoscale Prediction System (COAMPS; Hodur 1997), a regional relocatable atmospheric model, which in turns gets boundary conditions from the global Navy Operational Global Atmospheric Prediction System (NOGAPS; Goerss and Phoebus 1992; Rosmond 1992). The regional atmospheric model can be run at a user-defined horizontal resolution through a sequence of nests. Here, the COAMPS resolution is set to match the ocean model resolution of 2 km, and the forcing fields are archived and used in the model every 3 h. Open boundary conditions use a combination of radiative models and prescribed values provided by the parent nest. Different radiative options are used at the open boundaries depending on the model state variables: a modified Orlanski radiative model is used for the tracer fields (temperature and salinity), an advective model for the zonal velocity u, a zero gradient condition for the meridional velocity v as well as the barotropic velocities, and the Flather boundary conditions for elevation.

3. The 4DVAR system

a. The cost function

For the sake of clarity, the model equations given in the appendix in discretized form are rewritten in a simpler form here:

$$\begin{cases} \dfrac{\partial \mathbf{X}}{\partial t} = F(\mathbf{X}) + \mathbf{f}, & 0 \le t \le T \\ \mathbf{X}(t = 0) = \mathbf{I}(x) + \mathbf{i}(x) \end{cases}, \quad (1)$$

where $\mathbf{X}$ stands for all the dependent model state variables—two-dimensional sea surface height (SSH) and barotropic velocities, and three-dimensional temperature, salinity, and baroclinic velocities; F is the model tendency terms on the right-hand sides of (A1)–(A5) and (A10)–(A12) (see the appendix); $\mathbf{f}$ is the model error, a function of the independent variables (x and t) of the space–time domain Ω with covariance C_f; $\mathbf{I}(x)$ is the prior initial conditions; and $\mathbf{i}(x)$ is the initial condition error with covariance C_i. Given a vector $\mathbf{Y}$ of M observations of the model state in the space–time domain, with the associated vector of observation errors $\boldsymbol{\varepsilon}$ (with covariance $\mathbf{C}_\varepsilon$),

$$\mathbf{Y}_m = \mathbf{H}_m \mathbf{X} + \boldsymbol{\varepsilon}_m, \quad 1 \le m \le M, \quad (2)$$

where $\mathbf{H}_m$ is the observation operator associated with the mth observation, one can define a weighted cost function:

$$J = \int_0^T \int_\Omega \int_0^T \int_\Omega \mathbf{f}(x,t) \mathbf{W_f}(x,t,x',t') \mathbf{f}(x',t') \, dx' \, dt' \, dx \, dt$$
$$+ \int_\Omega \int_\Omega \mathbf{i}(x) \mathbf{W_i}(x,x') \mathbf{i}(x') \, dx' \, dx + \boldsymbol{\varepsilon}^T \mathbf{W}_\varepsilon \boldsymbol{\varepsilon}, \quad (3)$$

where Ω denotes the model domain; the weights $\mathbf{W_f}$ and $\mathbf{W_i}$ and are defined as inverses of C_f and C_i, respectively, in a convolution sense; and $\mathbf{W}_\varepsilon$ is the matrix inverse of $\mathbf{C}_\varepsilon$. The latter is usually considered to be a diagonal matrix, from the assumption that observation errors are uncorrelated. Boundary condition errors are omitted from (1) and (3) only for the sake of clarity. The model error covariance is assumed to take the form

$$C_f(x,t,x',t')$$
$$= \mathbf{v}(x)^{1/2} \mathbf{v}(x')^{1/2} \exp\left(-\frac{|x - x'|^2}{2L^2}\right) \exp\left(-\frac{|t - t'|}{\tau}\right), \quad (4)$$

where $\mathbf{v}(x)$ is the error variance and L and τ are the length and time scales, respectively. The initial error covariance C_i also assumes the form of (4) with the exception of the time correlation term and different (higher) variance. Horizontal correlations in (4) are obtained by solving a diffusion equation (Derber and Rosati 1989; Egbert et al. 1994; Weaver and Courtier 2001), while the time correlation is obtained by solving a pair of coupled Langevin equations (Chua and Bennett 2001; Bennett 2002; Ngodock 2005). Correlations in (4) are univariate and are implemented layer by layer for each model state variable. The cross correlations are provided by the model dynamics through the integration of the adjoint and the tangent linear models.

b. The minimization

The solution of the assimilation problem [i.e., the minimization of the cost function (3)] is achieved by solving the following Euler–Lagrange (EL) system:

$$\begin{cases} \dfrac{\partial \mathbf{X}}{\partial t} = F(\mathbf{X}) + C_f \cdot \boldsymbol{\lambda}, & 0 \le t \le T, \\[2mm] \mathbf{X}(t = 0) = \mathbf{I}(x) + C_i \circ \boldsymbol{\lambda}(x, 0) \\[2mm] -\dfrac{\partial \boldsymbol{\lambda}}{\partial t} = \left[\dfrac{\partial F}{\partial \mathbf{X}}(\mathbf{X})\right]^T \boldsymbol{\lambda} + \sum_{m=1}^{M} \sum_{n=1}^{M} W_{\varepsilon,mn}(\mathbf{y}_m - \mathbf{H}_m \mathbf{X}) \delta(x - x_m) \delta(t - t_m), & 0 \le t \le T \\[2mm] \boldsymbol{\lambda}(T) = 0 \end{cases}, \quad (5)$$

where $\boldsymbol{\lambda}$ is the adjoint variable defined as the weighted residual

$$\boldsymbol{\lambda}(x,t) = \int_0^T \int_\Omega \mathbf{W_f}(x,t,x',t') \mathbf{f}(x',t') \, dx' \, dt'$$

δ denotes the Dirac delta function, $W_{\varepsilon,mn}$ are the matrix elements of $\mathbf{W}_\varepsilon$, the superscript T denotes the transposition, and the covariance multiplication with the adjoint variable is the convolution

$$C_f \cdot \boldsymbol{\lambda}(x,t) = \int_0^T \int_\Omega C_f(x,t,x',t') \boldsymbol{\lambda}(x',t') \, dx' \, dt'$$

for the model error and

$$C_i \circ \boldsymbol{\lambda}(x,0) = \int_\Omega C_i(x,x') \boldsymbol{\lambda}(x',0) \, dx'$$

for the initial condition error. Note that, although the cost function is written with the inverse of the covariance functions, the actual inverses are not needed in the Euler–Lagrange equations in (5) associated with the minimization of (3).

1) GRADIENT DESCENT

By omitting the model error term in (1) or setting C_f to zero in (5), one recovers a familiar EL for strong constraint variational data assimilation that is solved by iterative algorithms such as the gradient descent. Starting from a first guess of the initial conditions, the nonlinear model is integrated forward in time and substituted into the adjoint model that is integrated backward in time, and from which the increments or corrections to the initial conditions are computed. The new initial conditions are used in a new iteration of the algorithm until the selected convergence criterion is satisfied. The same process can be used with the inclusion of the model error, except that the increase of the control space also

means the increase of the computational expense, and a potentially ill-conditioned minimization problem.

2) THE REPRESENTER METHOD

Allowing the model error increases the dimension of the control space and the computational cost of the assimilation and, usually, renders the minimization process poorly conditioned. This difficulty may be avoided if the minimization is done in the data space, which does not depend on, and is usually smaller than, the control space. That is possible through the representer algorithm, which expresses the solution of the EL system as the sum of a first guess and a finite linear combination of representer functions, one per datum. This cannot be applied to (5) directly mainly because of its nonlinear property. However, following Ngodock et al. (2000) and Bennett (2002), the representer algorithm can be applied to a linearized form of (5), which is obtained either by linearizing (5) directly or by linearizing the forward model (1) and deriving an EL associated with the cost function based on the linearized forward model. The iterative process by which the solution of the linearized EL becomes the background for the next linearization until formal convergence, is known as the "outer loop;" while the "inner loop" consists of actually solving the linear EL system. In either case, given a background model solution X^0 around which the model is linearized, one can write a linear EL system in the form

$$\begin{cases} \dfrac{\partial \mathbf{X}^k}{\partial t} = F(\mathbf{X}^{k-1}) + \left[\dfrac{\partial F}{\partial \mathbf{X}}(\mathbf{X}^{k-1})\right](\mathbf{X}^k - \mathbf{X}^{k-1}) + C_f \cdot \lambda, \quad 0 \le t \le T, \\[2mm] \mathbf{X}^k(t=0) = \mathbf{I}(x) + C_i \circ \boldsymbol{\lambda}(x,0) \\[2mm] -\dfrac{\partial \boldsymbol{\lambda}}{\partial t} = \left[\dfrac{\partial F}{\partial \mathbf{X}}(\mathbf{X}^{k-1})\right]^{\mathrm{T}} \boldsymbol{\lambda} + \sum_{m=1}^M \sum_{n=1}^M W_{\varepsilon,mn}(\mathbf{y}_m - \mathbf{H}_m \mathbf{X}^k)\delta(x-x_m)\delta(t-t_m), \quad 0 \le t \le T \\[2mm] \boldsymbol{\lambda}(T) = 0 \end{cases}, \qquad (6)$$

where k denotes the outer loop index and $\mathbf{X}^k$ is the EL solution after the kth outer loop. The EL system (6) is a linear coupled system between the adjoint and state variables. The representer method uncouples the system by expanding the solution as

$$\mathbf{X}^k(x,t) = \mathbf{X}_F^k(x,t) + \sum_{m=1}^M \beta_m^k r_m^k(x,t), \qquad (7)$$

where $\mathbf{X}_F^k$ is a first-guess solution, β_m^k are the coefficients, and $r_m^k(x, t), 1 \le m \le M,$ are the representer functions defined by

$$\begin{cases} -\dfrac{\partial \boldsymbol{\alpha}_m^k}{\partial t} = \left[\dfrac{\partial F}{\partial \mathbf{X}}(\mathbf{X}^{k-1})\right]^{\mathrm{T}} \boldsymbol{\alpha}_m^k + \mathbf{H}^{\mathrm{T}}\delta(x-x_m)\delta(t-t_m), \quad 0 \le t \le T \\[2mm] \boldsymbol{\alpha}_m^k(T) = 0 \\[2mm] \dfrac{\partial r_m^k}{\partial t} = F(\mathbf{X}^{k-1}) + \left[\dfrac{\partial F}{\partial \mathbf{X}}(\mathbf{X}^{k-1})\right] r_m^k + C_f \cdot \boldsymbol{\alpha}_m^k, \quad 0 \le t \le T \\[2mm] r_m^k(t=0) = C_i \circ \boldsymbol{\alpha}_m^k(x,0) \end{cases}, \qquad (8)$$
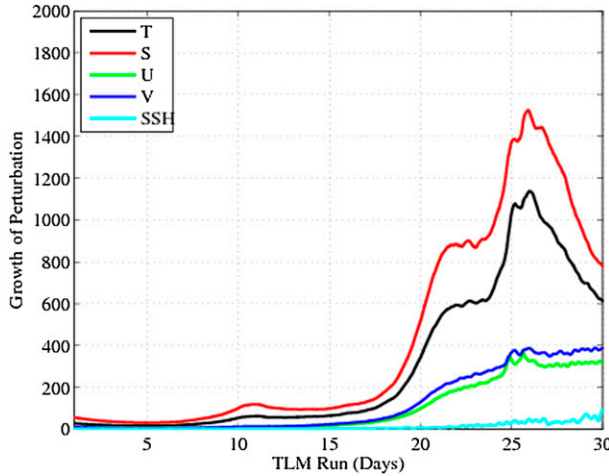
FIG. 1. Time evolution of the magnitude of the perturbation to the temperature, salinity, u, v, and SSH fields normalized by the magnitude of their respective initial perturbations.

FIG. 2. Vertical distribution of the magnitude of the model errors normalized by their surface value.

Note that the equations in (8) are only weakly coupled, since the $\boldsymbol{\alpha}_m^k$, also known as the adjoint representer functions, depend only on the observation locations and can be computed independently of the r_m^k. The first guess in (7) can be chosen as the previous outer-loop solution $\mathbf{X}^{k-1}$, or the tangent linear solution around $\mathbf{X}^{k-1}$. It may be shown that the representer coefficients are computed by solving a linear system in data space involving the representer matrix, the data error covariance matrix, and the innovation vector:

$$(\mathbf{R}^k + \mathbf{C}_\varepsilon)\beta = \mathbf{Y} - \mathbf{H}\mathbf{X}_F^k, \qquad (9)$$

where $\mathbf{R}^k$ is the representer matrix with elements $R_{mn}^k = r_m^k(x_n, t_n)$, that is, the mth representer function evaluated at the nth observation space–time location (x_n, t_n). The entire representer matrix need not be computed explicitly since the linear system (9) can be solved using an iterative algorithm (e.g., the conjugate gradient), by taking advantage of the symmetry of each matrix involved. Also, the representer coefficients constitute the right-hand side of the adjoint equation in the EL system. Thus, once the representer coefficients are computed, they are substituted into the adjoint equation, which is then solved and substituted into the forward linear equation for the final solution. A background solution around which the model is linearized is needed. Usually, it is the solution of the nonlinear model. For the first-guess solution, one may consider either the background or the tangent linear solution around the background. Also, the new optimal solution may replace the background for another minimization process (i.e., outer loops) until formal convergence (Bennett et al. 1996; Bennett 2002; Ngodock et al. 2000, 2007, 2009).
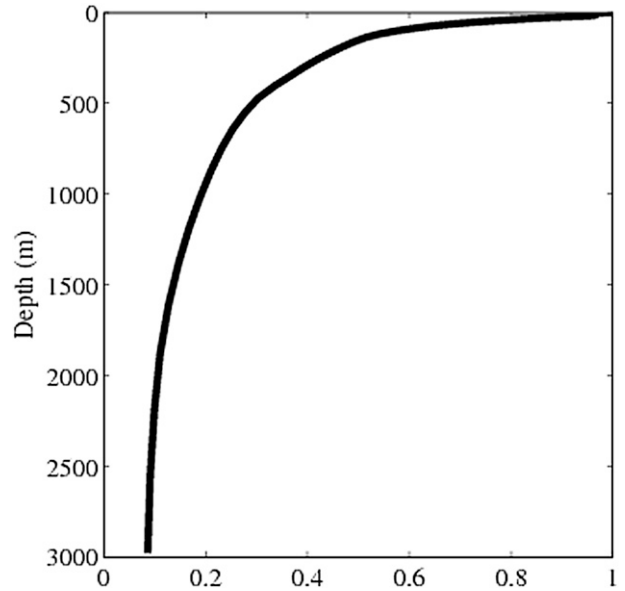
c. Linearization and adjoint derivation

The generation of both the tangent linear and adjoint codes of the model using the Parametric FORTRAN compiler (PFC; Erwig et al. 2007), including the symmetry test between the two codes, was described in Ngodock and Carrier (2013). Here, the stability of the linearized model is assessed by the time evolution of small perturbations: the tangent linear model is initialized by three-dimensional perturbations of the temperature, salinity, and velocity fields, as well as two-dimensional perturbations of the surface elevation field. These initial perturbations are generated randomly and assigned a magnitude of 2 K for temperature, 0.3 psu for salinity, 0.09 m s^{-1} for velocity, and 0.01 m for surface elevation. At each time step the norms of the perturbed fields are computed and divided by the norms of their respective initial perturbations. Results in Fig. 1, plotted every 6 h and starting 6 h into the integration, show that the linear perturbations are stable and bounded for about 16 days before they start to grow exponentially.

d. Error standard deviations: $\mathbf{v}(x)^{1/2}$

Assigning model errors and prescribing their covariances is the most difficult task in data assimilation (Daley 1992; Talagrand 1999; Bennett 2002; Wunsch 2006). Not only are there many error sources (external forcing, initial and boundary conditions, bad parameterization, empirical formulation, unresolved processes), but also the errors cannot be measured. Therefore, one can only make assumptions about them. Since NCOM
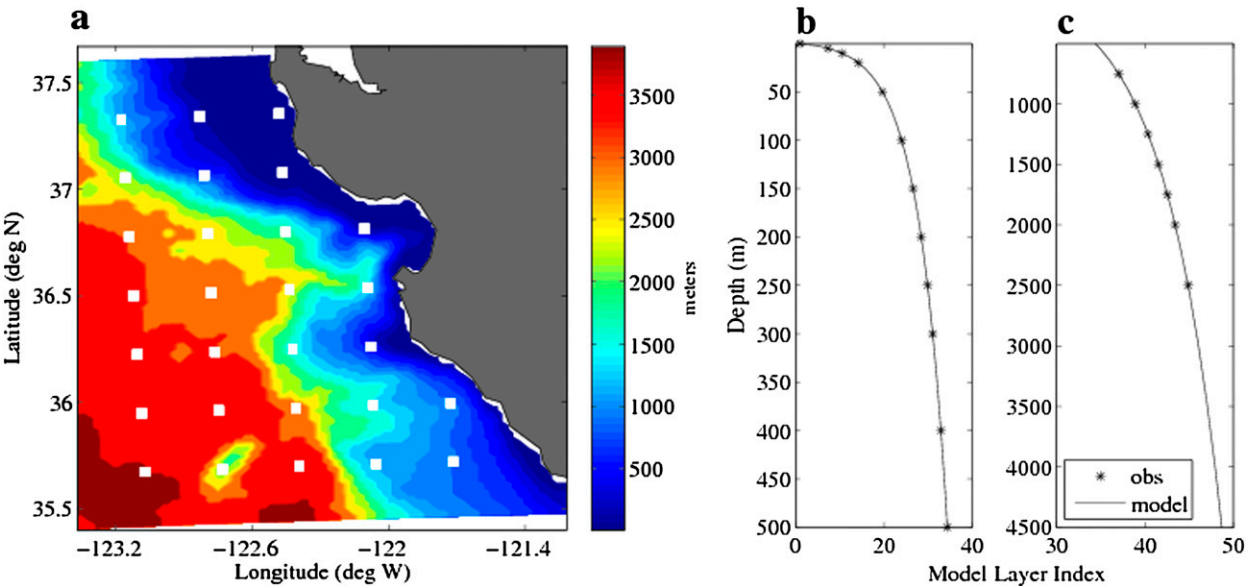
FIG. 3. (a) The model domain with bathymetry contours and the horizontal observation locations (white squares); the model layer index vs observation depths for (b) the upper 500 m and (c) below 500 m.

includes all resolvable processes and subgrid-scale parameterization, errors are attributed to the initial conditions and external forcing for all the dynamical equations, and the derivation of their estimates is given below. Note that there is no external forcing applied to the continuity equation, and thus it is not assigned a model error either, as in Jacobs and Ngodock (2003).

Consider the momentum equation in its nondiscretized form:

$$\frac{\partial \mathbf{u}}{\partial t} + \cdots = \cdots + \rho^{-1}\mathbf{F}/h, \qquad (10)$$

where $\mathbf{F}$ represents the wind stress atmospheric forcing (N m^{-2}), the volume flux source, or the tidal potential; h

is a typical water depth; and ρ is the water density. The model error at the surface consists of errors in the wind stress. For the subsurface, errors are assumed to arise from the volume flux and the tidal potential terms. Errors are considered to be high in magnitude at the surface and decreasing with depth. Although the wind stress varies in space and time, its associated error is assumed to be uniform in the horizontal directions. The error magnitude is considered to be 10% of the actual wind stress at the surface and decreasing with depth in order to mimic the decreasing impact of wind stress with depth. Two terms contribute to the forcing for the temperature equation: the net longwave, latent, and sensible heat fluxes on one hand, and the solar radiation

TABLE 1. List of all assimilation experiments and their associated settings indicated by the checked boxes.

|	Exp1	Exp2	Exp3	Exp4	Exp5	Exp6	Exp7	Exp8	Exp9
Wrong initial conditions	x	x	x	x	x		x	x	x
August forcing	x	x			x	x	x	x	x
July forcing			x	x					
30% forcing perturbation					x	x	x	x	x
2 × model error std devs				x					
Original simulated data sampling and error covariances	x	x	x	x	x		x	x	
Original simulated data sampling (surface only) and error covariances						x			
Twin data sampling and error covariances as in real-data experiments									x
3-day assimilation window							x		
Strong constraint	x						x	x	
Weakly strong constraint		x							
Weak constraint			x	x	x	x			x
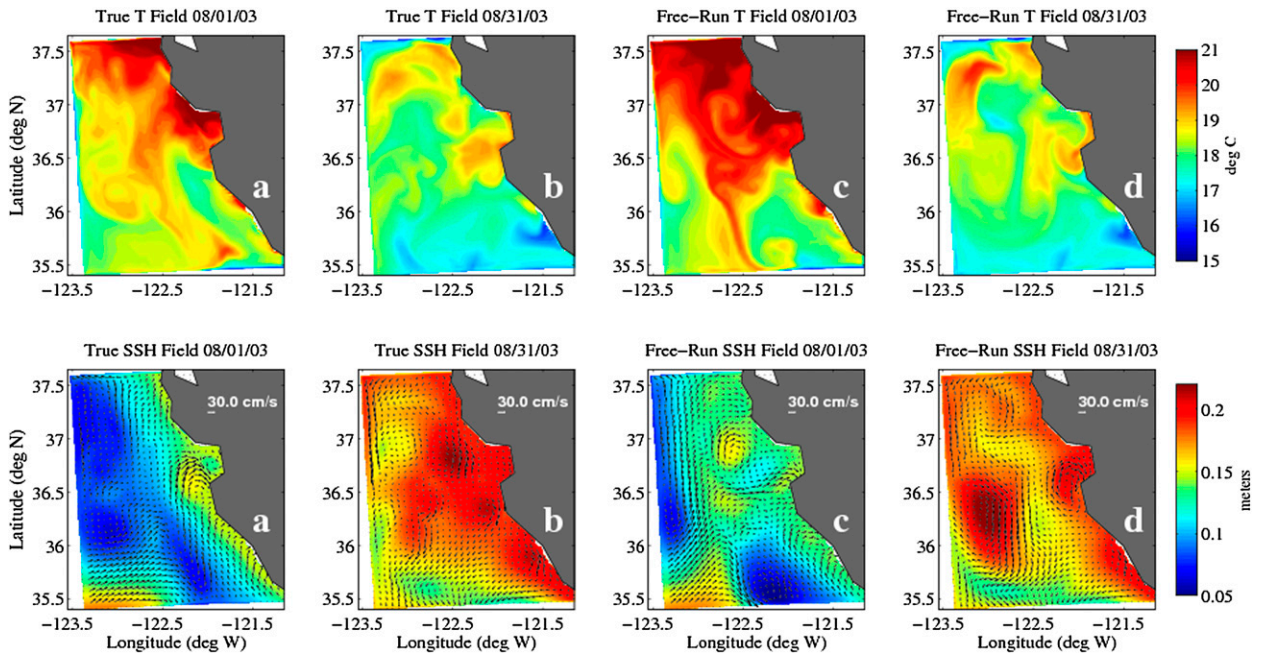
FIG. 4. (top) SST and (bottom) SSH with surface velocity vectors for the (a),(b) control and (c),(d) free-running solutions at the beginning and end of the assimilation window.

on the other hand. Both are assumed to be 10% in error and the sum of their errors constitutes the forcing error in the temperature equation, with a spatial distribution similar to the one used for the errors in the momentum equation. A similar approach is taken for the errors in the salinity equation, where the forcing consists of the river inflow and evaporation minus precipitation. Forcing terms here are also considered to be 10% in error.
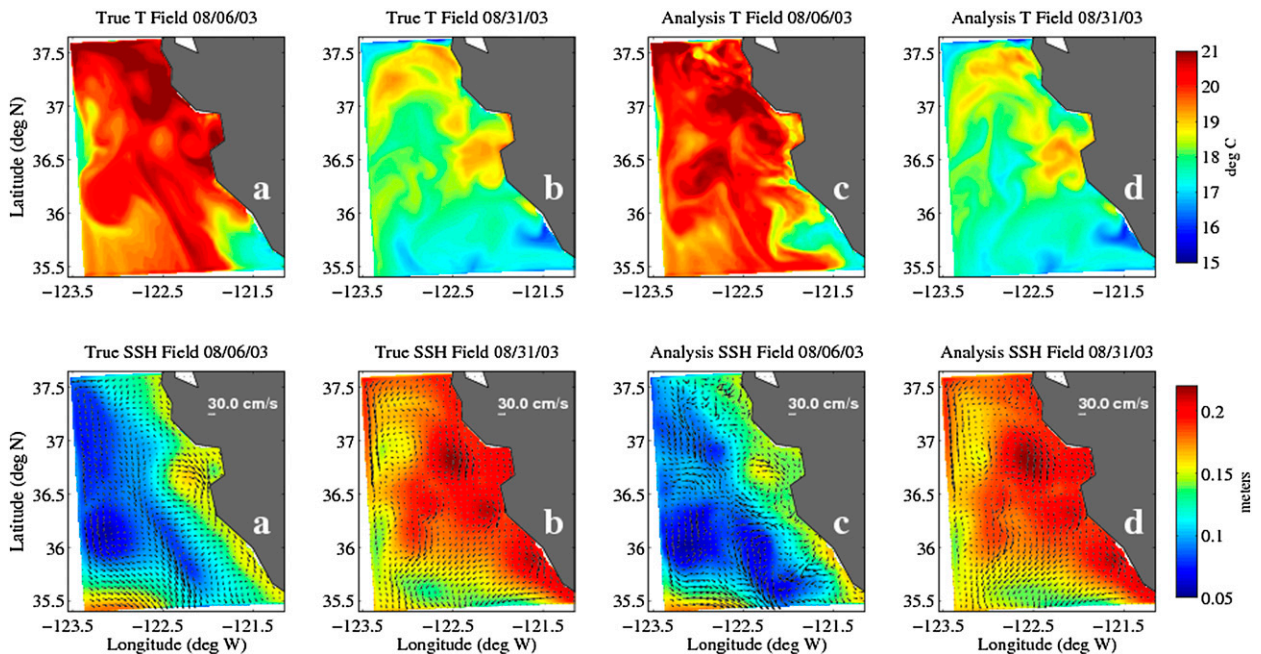
FIG. 5. As in Fig. 4, but for (c),(d) assimilated solutions at the end of the first cycle (6 Aug) and end of the assimilation window (31 Aug) from Exp1.
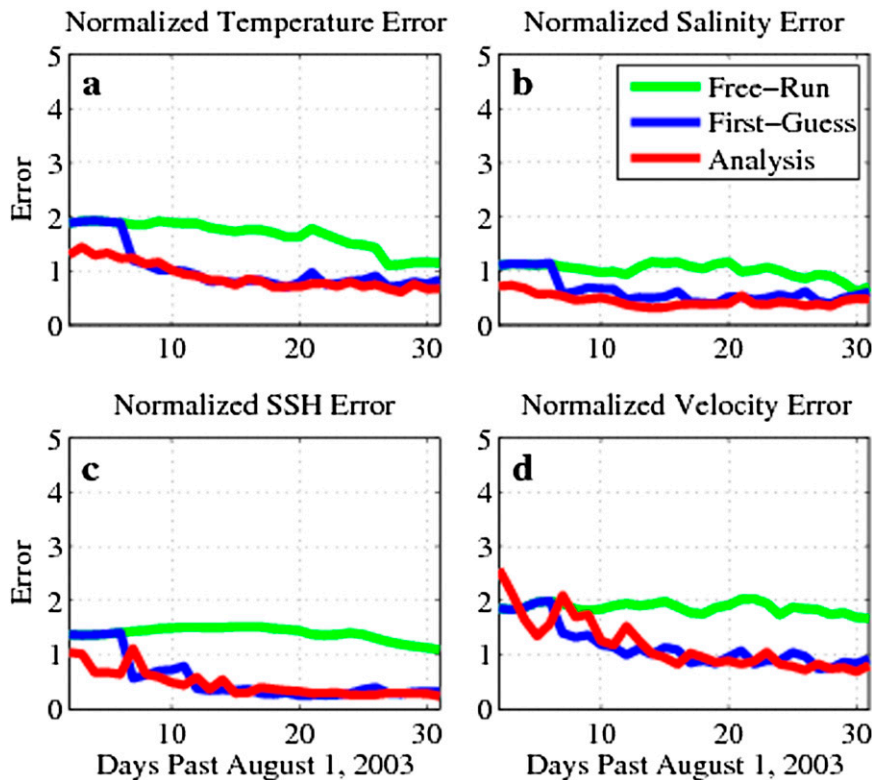
FIG. 6. Time series of the fit to the observations (red line) for (a) temperature, (b) salinity, (c) SSH, and (d) velocity.

The distribution of the model errors with depth in the momentum and tracer equations follows the normalized profile in Fig. 2, where errors at the surface have the 10% magnitude of the forcing described above. The spatial and temporal correlation scales in (4) are set to 20 km and 30 h, respectively.

4. Experiment setup and results

The model was initialized on 1 July 2003 and ran for 3 months to 30 September 2003. A portion of the model trajectory that corresponds to the time window 1–30 August is considered the control solution, and will also be referred to as the true solution or simply the "truth." Several 1-month-long assimilation experiments are carried out in order to evaluate the ability of the system to correct the initial conditions alone, the external forcing alone, both the initial conditions and external forcing, and the model error defined in the subsurface as a volume source.

A 1-month assimilation window is selected for 1–30 August, a time interval during which observations are sampled from the control solution. The simulated observations are saved and utilized in the 4DVAR analysis daily (i.e., at intervals of 24 h). There are 28 uniformly

distributed observation stations for SSH and profiles of velocity, temperature, and salinity across the model domain, as seen in Fig. 3. Each profile is represented on the model's vertical grid of 49 layers. Neighboring observations are separated horizontally from each other by 30 km. The temperature, salinity, velocity, and SSH observation errors are set to 0.4°C, 0.1 psu, 0.05 m s^{-1}, and 0.05 m, respectively, and are held constant through the entire assimilation window. These observation errors are purposefully set low to test the assimilation's ability to reduce large discrepancies with the model (i.e., to drive the model with large errors to fit observations with small errors). Within the month-long window, the assimilation is carried out in cycles of 5 days, where the analysis at the end of one cycle becomes the initial conditions for the next cycle. A total of nine assimilation experiments (summarized in Table 1) are carried out, using strong to weak constraints. They are designed to test several parameters of the assimilation system.

a. Controlling only the initial conditions

The wrong initial conditions are generated as follows: first, the solution on 5 July is used to restart the model on 15 July and, then, the model is integrated for 16 days
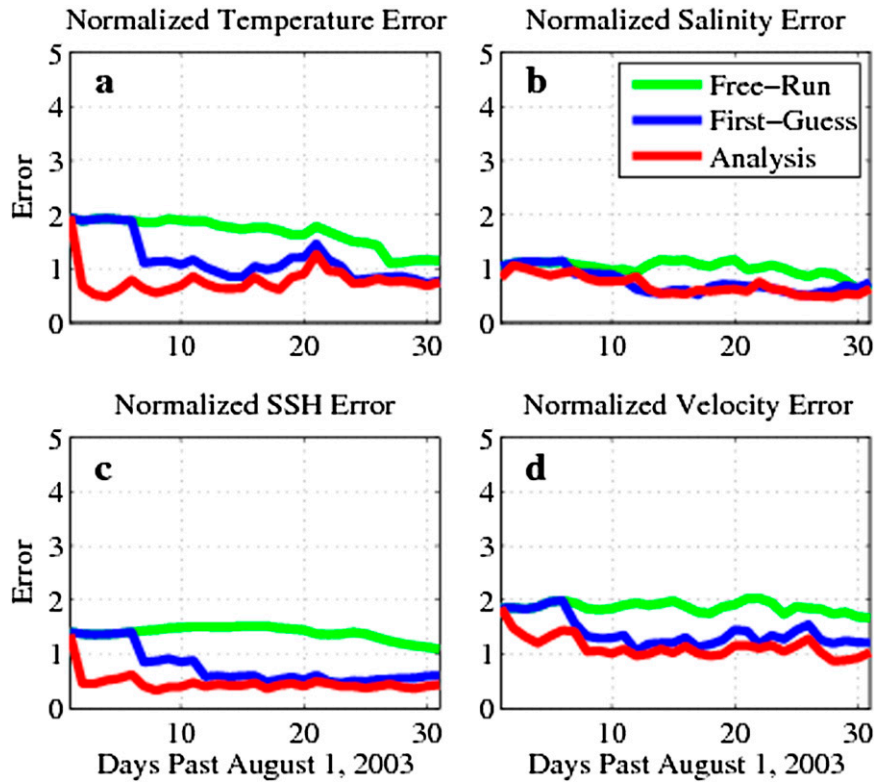
FIG. 7. As in Fig. 6, but for Exp2.

using the atmospheric forcing corresponding to 15–31 July. This yields a set of initial conditions on 1 August that are completely different from the control solution on the same date, and thus a solution for 1–31 August

that is different from the control solution for the same period, as seen in Fig. 4.

Because the difference between the two solutions is solely due to errors in the initial conditions, a strong
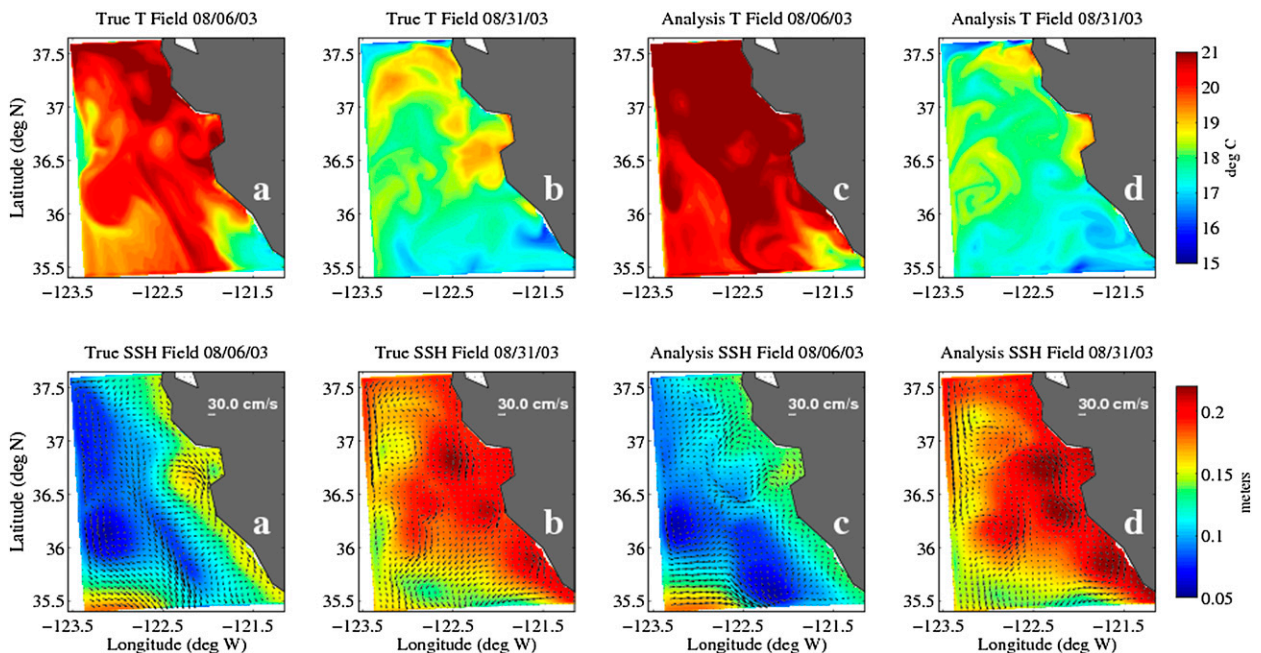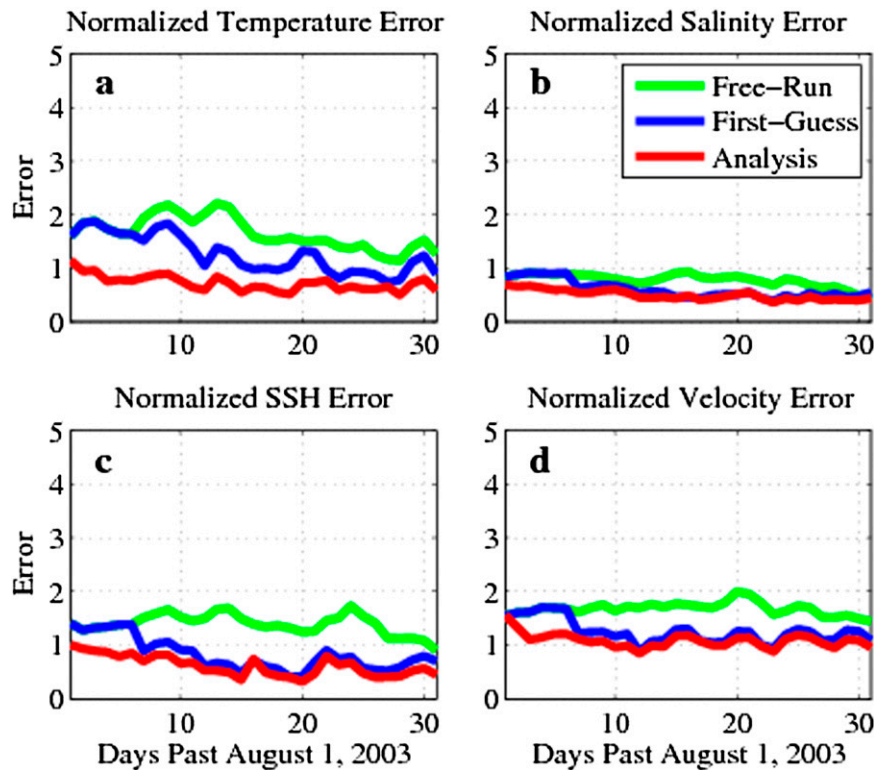

FIG. 8. As in Fig. 5, but for Exp3.

FIG. 9. As in Fig. 6, but for Exp3.

constraint assimilation approach is used (Exp1), in which the initial condition errors for temperature, salinity, velocity, and SSH are set to 2°C, 0.5 psu, 0.5 m s^{-1}, and 0.2 m, respectively. These initial condition (IC) errors are kept the same for the first two assimilation cycles, then progressively decrease by 20% every cycle after the second, as the assimilation is expected to improve the initial conditions for the following cycle. The IC errors are initially large to reflect the significant discrepancy between the free-running and the control solutions at the beginning of the assimilation window.

Results from the strong constraint assimilation in Fig. 5 show that there are still some noticeable differences between the assimilated and the control solutions after the first cycle, especially in the SSH and surface velocities. However, by the end of the assimilation window (i.e., after the sixth cycle), the differences between the two solutions are minor and, for the most part, within the respective observation errors. This is confirmed by the fit to the observation metric:

$$J_{\text{FIT}} = \frac{1}{M} \sum_{m=1}^{M} \frac{|\mathbf{y}_m - \mathbf{H}_m \mathbf{X}^a|}{\boldsymbol{\sigma}_m}, \qquad (11)$$

where $\mathbf{y}_m$ is the mth observation, M is the number of observations, $\mathbf{H}_m$ is the observation operator, $\mathbf{X}^a$ is the

assimilated solution or analysis, and $\boldsymbol{\sigma}_m$ is the observation error. The right-hand side of (11) is computed as a time series for each observation type, and also evaluated for the free-run solution and the first guess. The latter is the forecast obtained by integrating the nonlinear model for 5 days, initialized by the analysis at the end of the cycle.

Because the assimilation is expected to fit the observations to within the observation standard deviations, the right-hand side of (20) is expected to be less than one for the analysis, but not necessarily for the first guess. It can be seen in Fig. 6 that the free-running solution is far from the observations, by as much as two standard deviations in temperature end velocity, due especially to the wrong initial conditions being chosen. In general, the assimilation fits the observations within a standard deviation, except for the temperature in the first cycle and the velocity in the first three cycles. There is also a significant improvement in the forecast, which remains within an observation standard deviation after the first two cycles. After the first cycle, forecast (and thus analysis) errors remain low due to the right forcing, except in the velocity. The latter display some inaccuracies resulting from the end of the first cycle that negatively affect both the forecast and the analysis in the second cycle. However, the
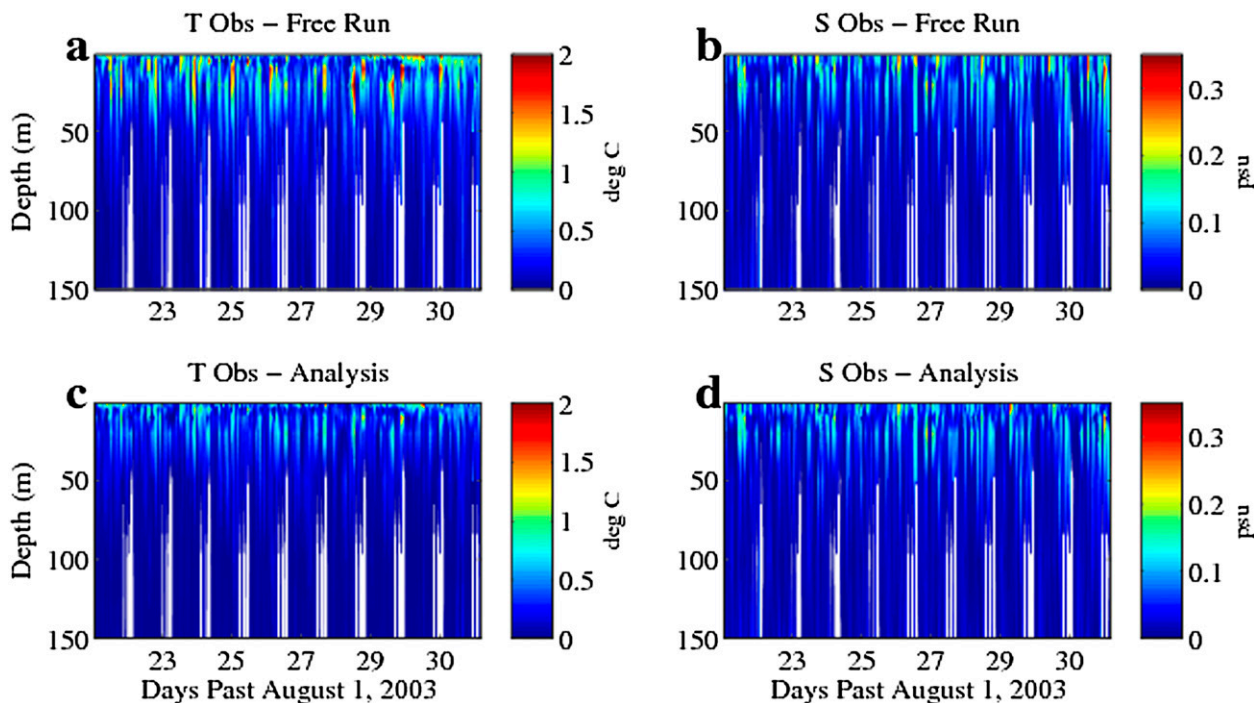
FIG. 10. Profile time series of (a),(c) absolute temperature and (b),(d) salinity differences with the true solution from the (top) free-running and (bottom) Exp3 solutions.

assimilation corrects those inaccuracies in the third and subsequent cycles.

WEAKLY STRONG CONSTRAINT

It is also possible to carry out a strong constraint experiment within the representer method by setting the model error term to zero in the linearized EL. This experiment is referred to as the weakly strong constraint (Exp2), because the correction of the model trajectory is based on the linearized dynamics [see (6)] contrary to the original strong constraint that uses nonlinear dynamics. The weakly strong approach has the potential to be computationally less expensive when the number of observation being assimilated is significantly less than the dimension of the initial conditions. The fit to the observations metric plot in Fig. 7 shows that the weakly strong constraint assimilation fits the observations similarly well compared to the strong constraint. There is a faster decrease of the analysis error in the first two cycles, with the exception of salinity. There is also a slight increase in the analysis error in temperature (fifth cycle) and velocity (fifth and sixth cycles). The differences in the curves from Figs. 6 and 7 are mostly due to the fact that the correction of the model trajectory in the strong constraint uses nonlinear dynamics, whereas linearized dynamics are used in the weakly strong constraint.

b. Weak constraint: Controlling IC and forcing

In the third experiment (Exp3), the assimilation is carried out with the wrong initial conditions used in the experiments above and incorrect forcing (described below) using the representer method. The experiment is set up by running the model in the second month using the wrong initial conditions for the strong constraint experiment above, and the 30-day atmospheric forcing starting from 1 July. This rather drastic choice of the wrong forcing (just as with the wrong initial conditions in the strong constraint experiment) is intended to test the robustness of the assimilation system. Usually, a perturbation is added to the true forcing. The initial condition errors are the same as those of the strong constraint experiment, and the model errors are as described in section 3c. Results of assimilating with wrong ICs and forcing fields show that for surface fields (temperature, height, and velocity) in Fig. 8, the assimilated solution has substantial inaccuracies after the first cycle, although the solution shows much better agreement with the truth at the end of the last cycle.

The fit to the observations metric in Fig. 9 shows that the assimilation is fitting temperature, salinity, and SSH within respective standard deviations, and the fit to velocity is borderline with the standard deviation. In Fig. 8
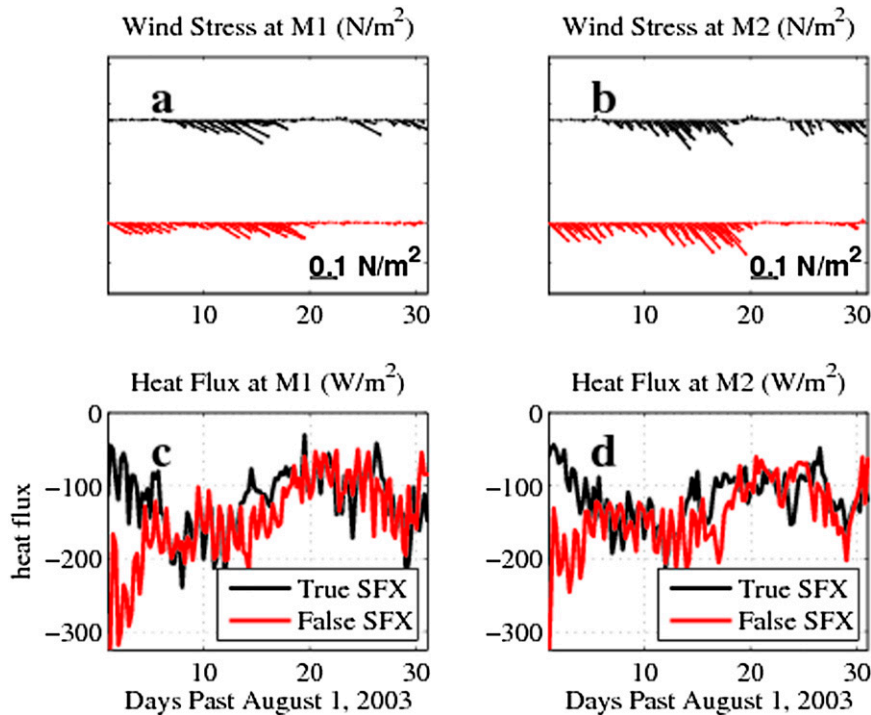
FIG. 11. Time series of (a),(b) surface wind stress and (c),(d) heat flux for the months of July (red lines) and August (black lines) at the (left) M1and (right) M2 buoys in Monterey Bay. The August forcing is the true forcing.

errors of about 1 K (two standard deviations) still remain in the surface temperature, which seems to contradict the metric in Fig. 9. The latter, however, is an average that does not reveal the inaccuracies of Fig. 9 due to there being a better fit to the observations in the lower layers. This is shown in Fig. 10, where it can be seen that both temperature and salinity errors from the free run extended to more than 100 and 50 m, respectively. Assimilation errors are significantly reduced in magnitude and do not extend below 50 m. That the remaining errors in the assimilation are confined near the surface may be due to the drastic choice of wrong forcing fields and rather small standard deviations for the model error terms.

The time series of the wind stress and heat flux for the true and erroneous July forcings are shown in Fig. 11 at the locations of the M1 and M2 buoys in Monterey Bay. The forcing fields display large differences in the first 7 and the last 11 days of the assimilation window. In between those days, the wind stress generally is in the same direction in both forcings, but differences persist in the magnitude. Expressing the July forcing in error percentage shows that on average it is, relative to the true forcing, more than 100% in error over all the model domain.

In light of the significantly high errors in the July forcing and the very low standard deviations in the assimilation, this weak constraint experiment is repeated in two ways. First, the July forcing is used in the assimilation while the model error standard deviations are increased by a factor of 2 (Exp4). Note that these standard deviations are still significantly lower than the actual errors that the July forcing brings into the system. Second, perturbed forcing fields (instead of the 1-month delayed case) representing 30% of the July forcing are added to the true forcing, and the assimilation is carried out with the 10% errors prescribed earlier (Exp5).

Assimilation results from these experiments are shown in comparison to the original weak constraint experiment (Exp3) for temperature profiles and surface velocity and height. It is shown in Fig. 12 that when the assimilation is carried out with the wrong July forcing, the quality of the analysis slightly improves as the model error standard deviations are increased by a factor of 2, from 10% to 20%. This result shows that the assimilation system is able to overcome significantly high errors in the forcing to correct the model trajectory in each cycle with significantly low model error specifications. The results of the assimilation get even better when the forcing error is dropped to 30%, while keeping the model
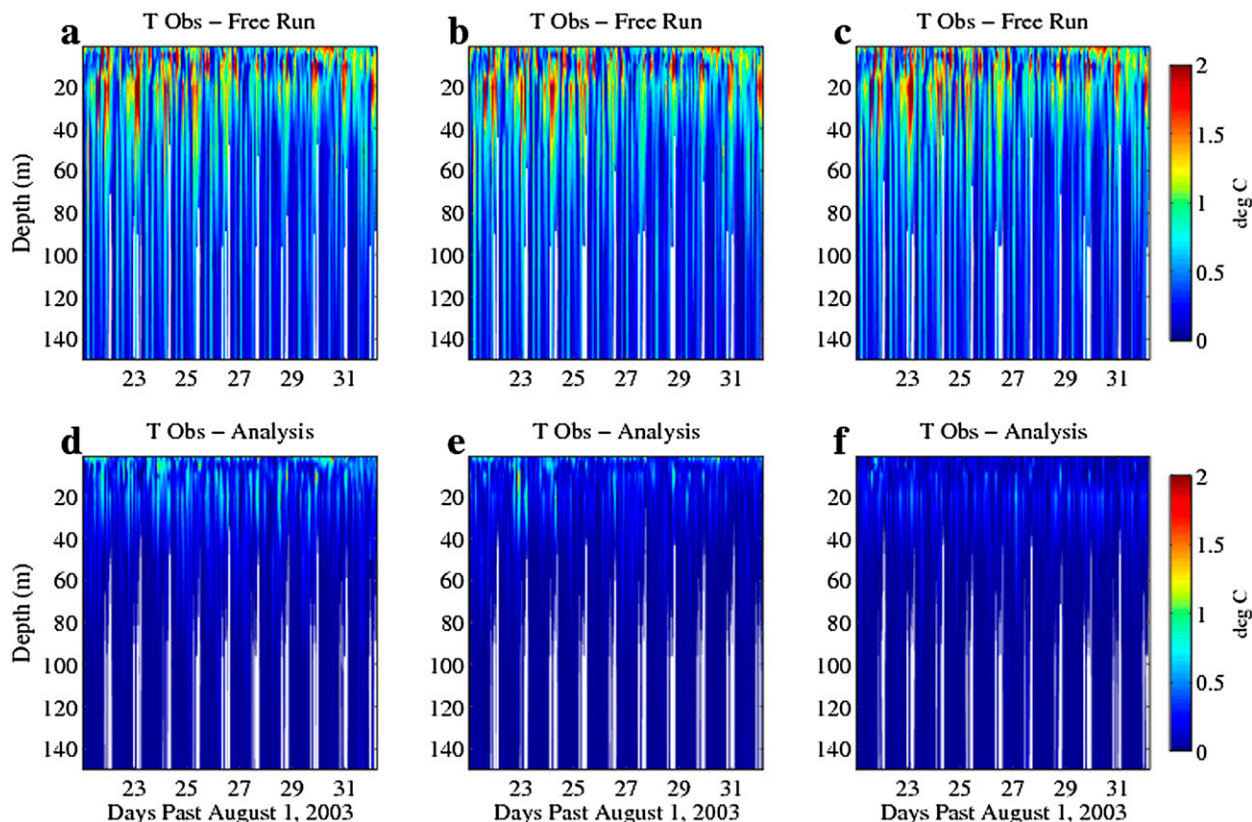
FIG. 12. Profile time series of temperature differences (a)–(c) between the true solution and the free run and (d)–(f) between the true and assimilated solutions from (left) Exp3, (center) Exp4, and (right) Exp5. Time series are shown for the last two cycles.

error to 10%. That is, when the model error is set to relatively similar levels as the actual errors, the assimilation fits the observations with greater accuracy. Similar results are obtained with salinity profiles (not shown).

The improvement of the assimilation is also assessed for the analyzed SSH and surface velocities by looking at the difference of these fields between the truth and the analysis from the three weak constraint experiments. As
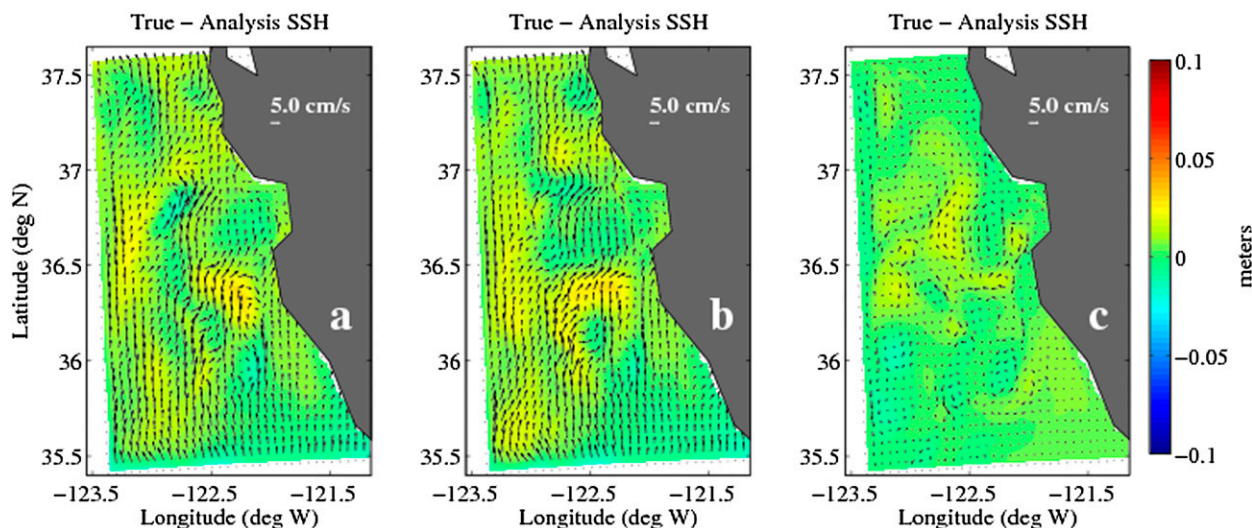

FIG. 13. SSH and surface velocity vector differences between the truth and (a) Exp3, (b) Exp4, and (c) Exp5, on 21 Aug.
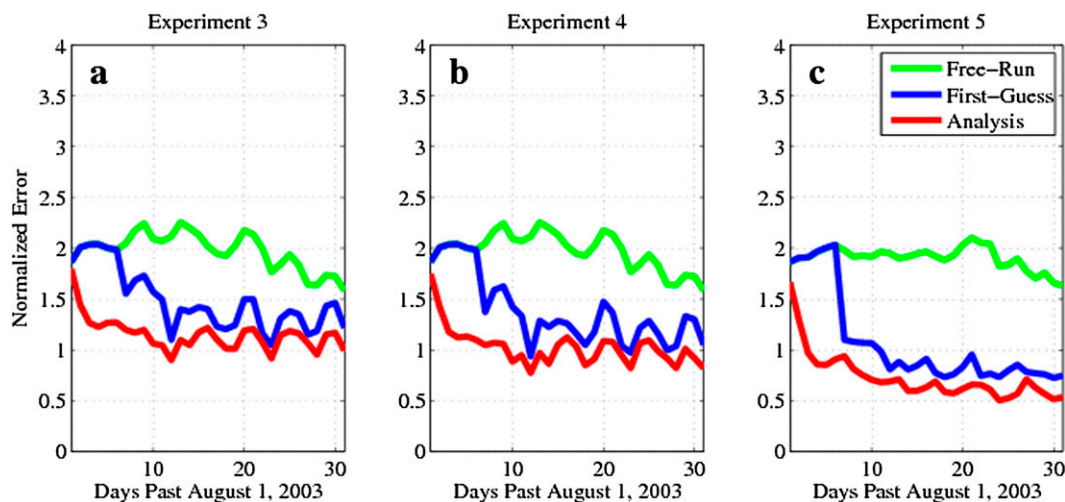
FIG. 14. Time series of the fit to the observations metric from (a) Exp3, (b) Exp4, and (c) Exp5.

can be seen in Fig. 13, the analysis errors of these surface fields are similar between the original weak constraint experiment and the one with doubled model error standard deviations, and the analysis error is much lower for the experiment with 30% perturbation on the forcing and the model error standard deviations set at 30%.

The overall assimilation performance is shown in Fig. 14 as the fit to the observations metric. Unlike similar figures shown above for individual observation types, the metric in Fig. 14 combines all observations. It confirms the assessment of the three weak constraint experiments described above for the temperature
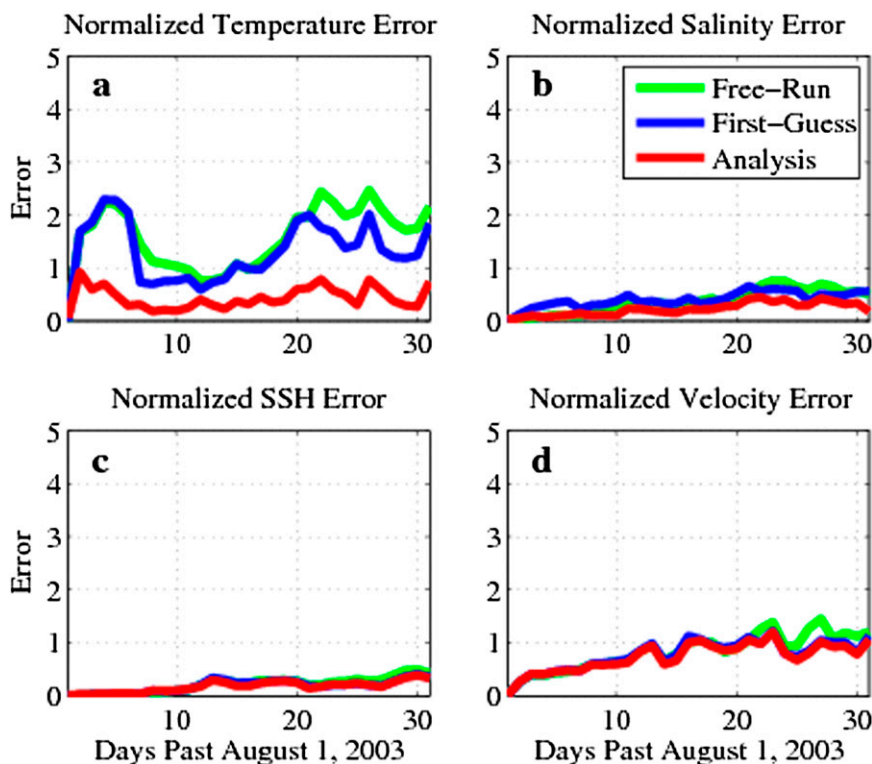

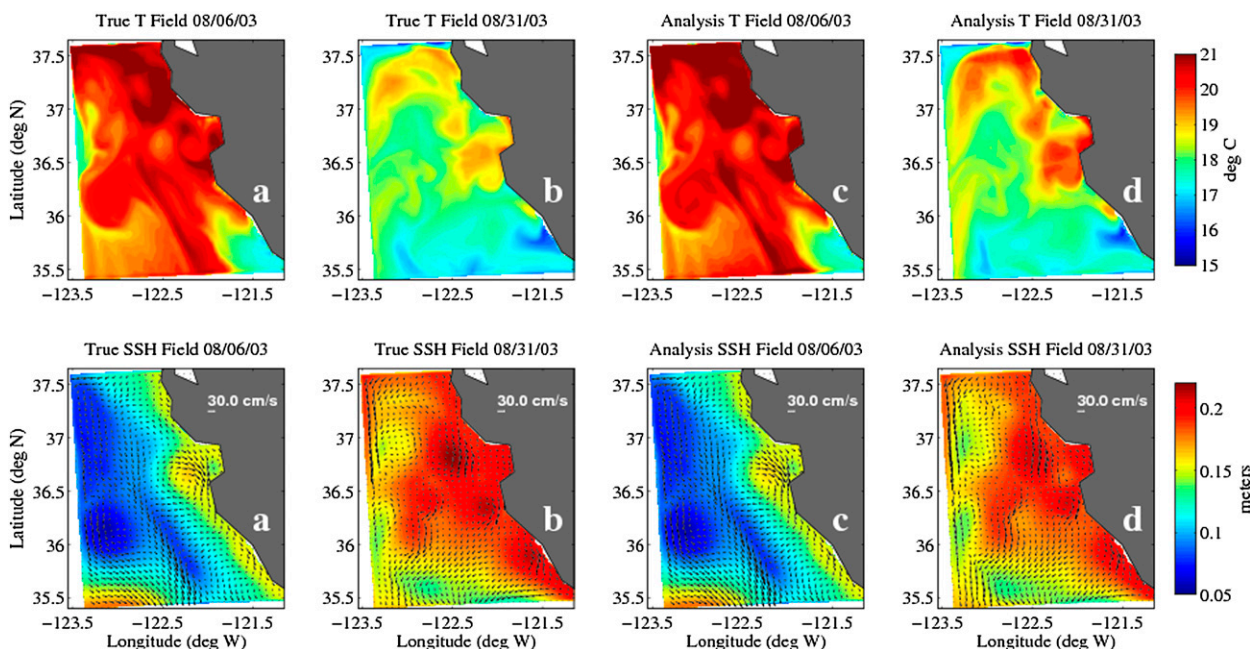
FIG. 15. As in Fig. 6, but for Exp6.

FIG. 16. As in Fig. 5, but for only Exp6.

profiles and the surface height and velocity. 1) The original weak constraint assimilation experiment with the wrong July forcing and only 10% model error standard deviations is able to correct the model trajectory and steer it toward the observations so that by the end of the first cycle the analysis error is within the observations standard deviation. The associated forecast is also significantly improved; from the third cycle and forward, the forecast error is about an observation standard deviation. 2) There is a marginal improvement (slightly lower analysis error) of the assimilation by increasing the model error standard deviations by a factor of 2, as well as a marginal improvement of the 5-day forecast. 3) Moreover, the improvement of the assimilation is quite significant for the experiment with 30% perturbation of the forcing and 10% model error standard deviations, from the second cycle onto the last. The same is true for the 5-day forecast associated with this assimilation experiment.

c. Forcing alone

It may be argued that the experiments with the wrong July forcing are fitting the observations within the observation standard deviation because of the contribution of the subsurface where forecast and analysis errors are significantly lower than at the surface, and the 5-day cycle length is not long enough for the wrong surface forcing to drastically and adversely impact the forecast.

A sixth experiment (Exp6) is set up that seeks to correct only the external surface forcing by assimilating only surface observations. This experiment uses correct initial conditions, the 30% perturbation on the forcing, and the 10% model error standard deviation prescribed only at the surface. According to Fig. 11, the 30% forcing perturbation produces errors that are most noticeable in the heat flux and, therefore, in the surface temperatures. The fit to the observations metric for this experiment shows, in Fig. 15, that for salinity and SSH, both the free-run and forecast errors are always within an observation standard deviation and, thus, the analysis. The same is true for velocity until the last two cycles, where the free-run errors increase to slightly more than a standard deviation, and the assimilation subsequently corrects them. The major impact of the assimilation is in the surface temperature, where errors as high as two observation standard deviations in the free run and the forecast are reduced to less than a standard deviation in the analysis.

Surface temperature, elevation, and velocity fields (at the end of the first and the fourth cycles) in Fig. 16 show that the assimilation accurately recovers all the circulation features, albeit for slightly higher temperatures at isolated locations. Although these temperature inaccuracies may be as high as 1 K, they are isolated in the sense that they do not dominate the overall fit to the observations metric shown in Fig. 15.

Actual forcing errors and the retrieved errors from the assimilation are compared at the end of the first and fourth cycles in Fig. 17. It can be seen that the assimilation does not recover the wind stress errors: corrections to the
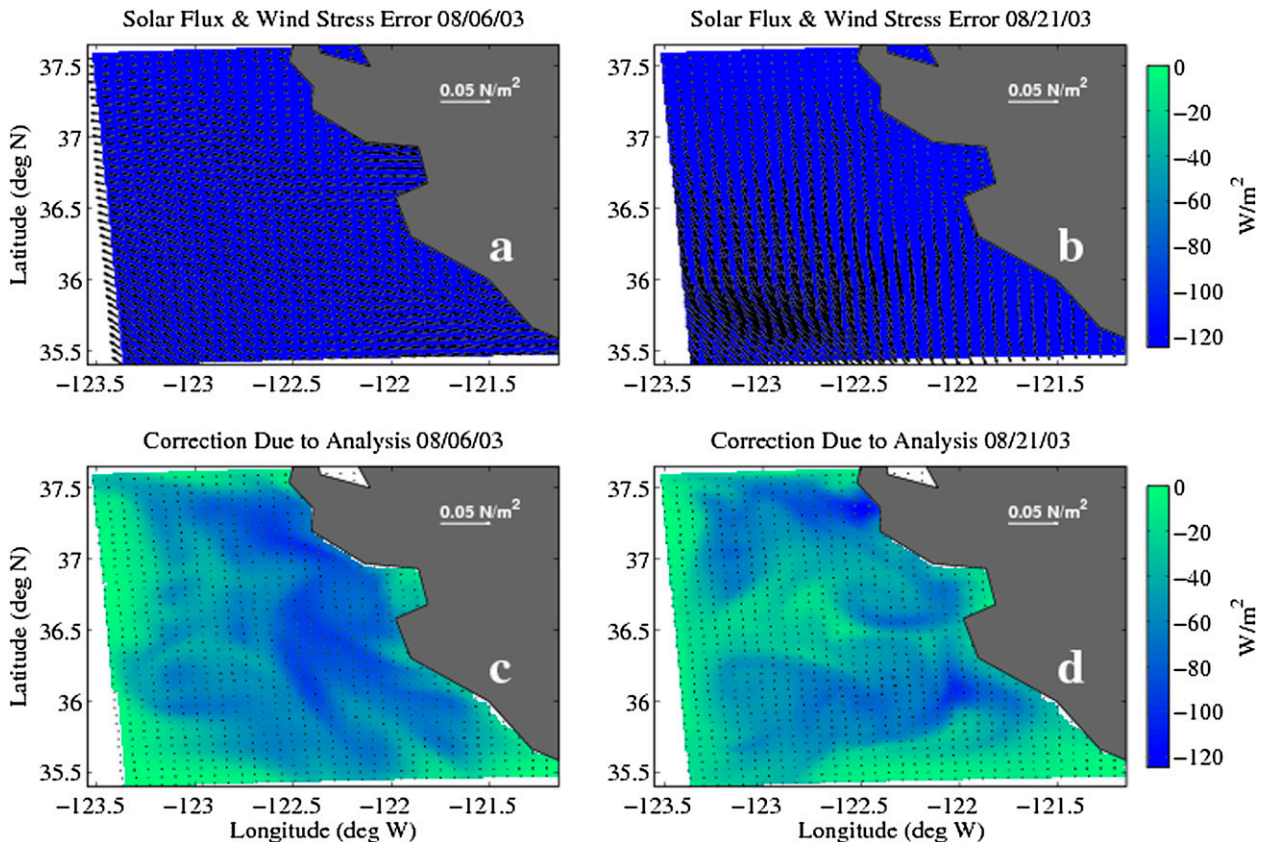
FIG. 17. (top) Actual and (bottom) retrieved errors in the surface heat flux and wind stress at the end of the (a),(c) first and (b),(d) fourth cycles.

wind stress are negligible compared to the actual errors. The assimilation corrects the heat flux better than it does the wind stress, even though the magnitude of the correction is lower than the actual errors. It should be emphasized that the assimilation used model error standard deviations at 10% of the actual forcing fields, while the actual errors were set at 30%. The discrepancy in error levels explains in part the difference between the retrieved and actual errors.

d. Shorter cycle strong constraint

In the seventh experiment (Exp7), we investigate the possibility of improving the performance of the strong constraint assimilation by resorting to a shorter assimilation window. This idea seems reasonable from the tangent linear model (TLM) point of view: the tangent linear approximation underlying the variational method is more accurate and thus more stable over a shorter cycle. It should be noted, however, according to Fig. 1 in section 3, that the TLM stability exceeds 10 days for initial perturbations. Therefore, the original strong constraint experiment (Exp1), which used an assimilation window of 5 days, could not have been negatively affected by linear error growth, and a strong constraint experiment with an assimilation window shorter than 5 days should not yield better results. To verify this, Exp7 is set up just as in Exp1, but with a 3-day assimilation window.

Results in Fig. 18 show that there is no substantial improvement from the 5- to the 3-day strong constraint assimilation windows, except for the velocity in the first half of the month-long experiment. Note that in that first half neither Exp1 nor Exp7 fits the observations to within a standard deviation. Once that begins to happen in the second half of the month, both experiments have the same accuracy.

e. Strong constraint with forcing errors

The strong constraint performance is further investigated within the context of both initial conditions and forcing errors. This follows the design of Exp5 with the only exception that the assimilation is carried out with strong constraint using the representer method. The results of Exp8 are shown in Fig. 19, where the
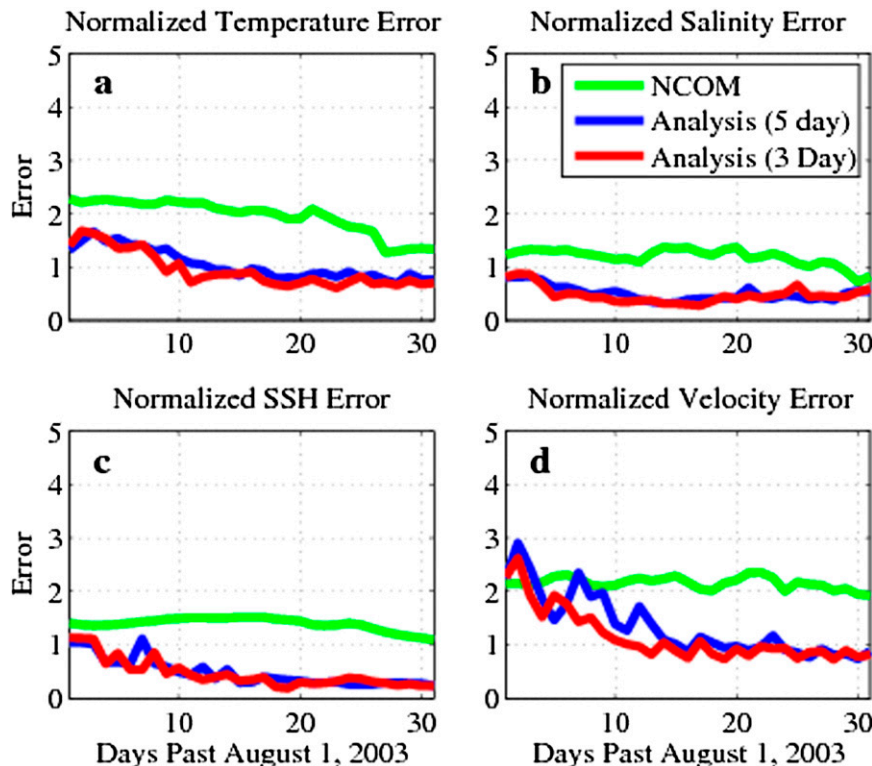
FIG. 18. As in Fig. 6, but for comparison between the free run and analyses from Exp1 and Exp7.

strong and weak constraint analyses are compared. It can be seen that the weak constraint assimilation fits the observations better than the strong constraint, owing to its higher number of degrees of freedom. It is expected of the strong constraint to correct the model trajectory by adjusting the erroneous initial conditions. However, if the model is driven by an erroneous forcing, the latter will steer the model trajectory away from the observations even if the initial conditions were perfectly corrected. This is seen in Fig. 19, especially for the temperature and velocity, by the decrease of the analysis error at the beginning of the each cycle followed by a gradual increase. It should also be noted that the strong constraint fits the salinity and SSH observations well, although not as well as the weak constraint. This can be attributed to the facts that salinity forcing is poorly known and as such its perturbations for forcing errors are small, and there is no forcing perturbation for the SSH equation because it is treated as a conservative quantity.

f. Sampling at real observation locations

In most of the experiments above, the assimilation experiments are assessed at the observation locations. However, the availability of the true solution makes it possible to evaluate the ability of the assimilation to correct the model everywhere else in the domain. A weak constraint assimilation experiment (Exp9) is carried with data sampling and error settings as in the real-data experiments described in the second part of this paper (Ngodock and Carrier 2014, hereafter Part II), and a comparison to the true solution over the entire domain is made to assess the assimilation's ability to reconstruct the true solution away from the assimilated observations. Exp9 is run for a 60-day window (in 5-day cycles) to allow the dynamics to propagate the assimilation corrections through the model domain. In Fig. 20 the normalized global differences (in the three space dimensions) between the weak constraint and true solutions are compared.

It can be seen that initially the assimilation does not compare well to the true solution for all of the variables. The errors in the salinity and SSH fields are lower than those in the temperature and velocity fields, probably due to the same reasons mentioned above for Fig. 19. But as time progresses, the model dynamics are able to propagate the assimilation corrections through the model domain and the discrepancy between the assimilation and true solution decreases: salinity and SSH errors become lower than 1 standard deviation; temperature errors are close to 1 standard deviation, having started around 2.0 standard deviations; and finally velocity errors have
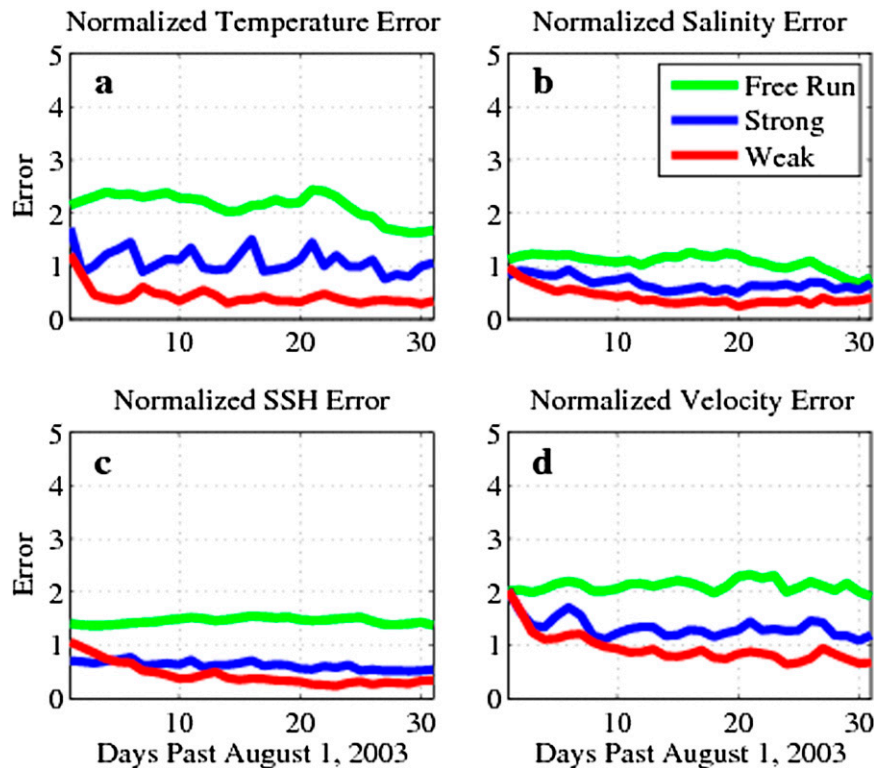
FIG. 19. As in Fig. 6, but for comparison between the free-run and analyses from Exp5 and Exp8.

decreased to 1.5 standard deviations having started at 2.5. It is arguable that these errors would have decreased further to below a standard deviation; that is, the assimilation would eventually reproduce the true solution in the entire region had the system run long enough.

5. Conclusions

A 4D variational system was developed for assimilating ocean observations with the Navy Coastal Ocean Model. The system is described in this paper, along with initial assimilation experiments in Monterey Bay using synthetic observations. The assimilation system is tested in a series of twin data experiments to assess its ability to fit assimilated and independent observations by controlling the initial conditions and/or the external forcing while assimilating surface and/or subsurface observations. The minimization of the cost function was done with the gradient descent method in all of the strong constraint experiments, and with the representer method (observation space) in the weak constraint experiments.

It was shown that in the strong constraint approach the system is able to correct wrong initial conditions to

fit the observations within a standard deviation after two 5-day cycles. After the first cycle, forecast (and thus analysis) errors remain low due to the right forcing, except in the velocity. The latter displays some inaccuracies at the end of the first cycle that negatively affect both the forecast and analysis in the second cycle. However, the assimilation corrects those inaccuracies in the third and subsequent cycles. The length of the strong constraint assimilation window was reduced to explore the possibility of improving its performance. It was noted that since the TLM was shown to be stable beyond 10 days, a shorter than 5-day assimilation window would not improve the accuracy of the strong constraint, and that was confirmed by an actual assimilation experiment. Finally, the strong constraint was compared to the weak constraint in the case of wrong initial conditions and forcing. It was shown that although the strong constraint could accurately correct the initial conditions, the wrong forcing would keep steering the solution away from the observations; only the fields that had low forcing perturbations (salinity) or none (SSH) could be accurately fit by the assimilation.

Several weak constraint experiments were carried out. First, a completely wrong forcing was used in the
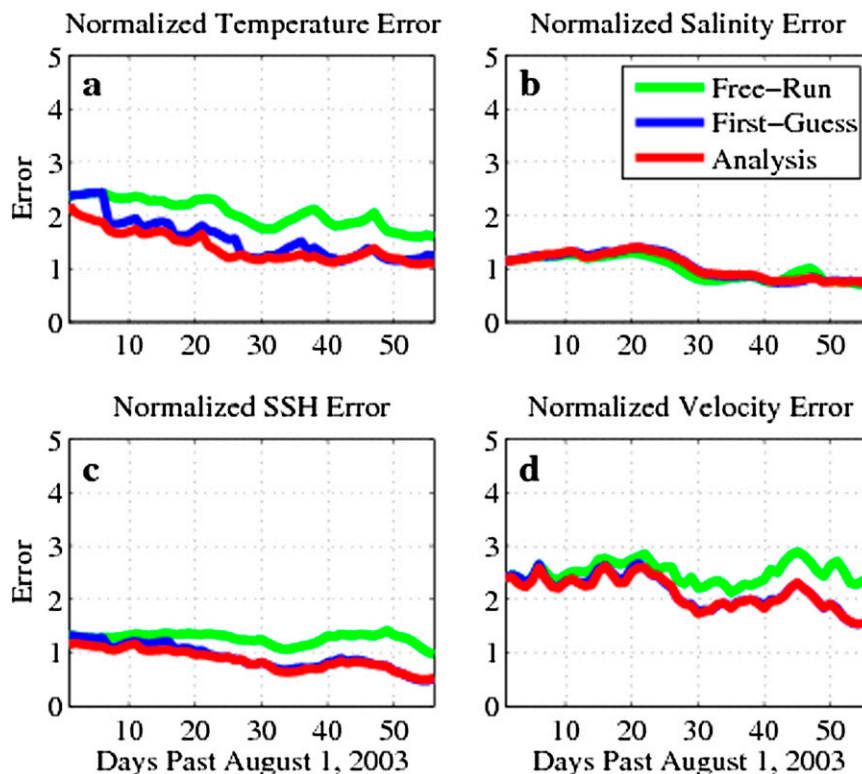
FIG. 20. As in Fig. 6, but for normalized global differences (in the three space dimensions) between the true solution and Exp9 (red lines), the first guess (blue lines), and true free-run (green lines) solutions.

free run and forecast, while model error standard deviations were set to 10% of the magnitude of the true forcing. In general, the assimilation was able to fit the observations, although some isolated discrepancies greater than twice the observations' standard deviation remained in the analysis. This was mostly due to high actual forcing errors and very low model errors for the assimilation. The second weak constraint experiment followed the first, except with doubled model error standard deviations in the assimilation. There was a marginal improvement in the analysis, as the difference between the actual forcing errors and the prescribed model errors in the assimilation remained high. In the third weak constraint experiment, forcing errors were computed as a 30% perturbation of the true forcing, and the model error standard deviations were kept at 10%. There was a significant improvement in the accuracy of the analysis compared to the first two weak constraint experiments. The fourth weak constraint experiment follows the third, except only surface observations were assimilated and the model errors were also restricted to the surface. This experiment yielded accurate surface fields, and the forcing corrections showed that the assimilation corrected the

heat flux better than it did the wind stress, even though the magnitude of the corrected fluxes was lower than the actual errors. This resulted from using smaller model error standard deviations (a third of the actual errors magnitude) in the assimilation. The assimilation system is able to overcome significantly high errors in the forcing to correct the model trajectory in each cycle with significantly low model error specifications. The results of the assimilation get even better when the forcing error is dropped to 30%, while keeping the model error to 10%. That is, when the model error is set to relatively similar levels as the actual errors, the assimilation fits the observations with greater accuracy. There was a discrepancy between the actual forcing errors and the retrieved forcing errors from the assimilation that is explained in part by the difference between the actual and prescribed error magnitudes in the assimilation.

Finally, a weak constraint assimilation experiment was carried with data sampling and error settings as in the real-data experiments described in Part II, and a comparison to the true solution over the entire domain was made to assess the assimilation's ability to reconstruct the true solution away from the assimilated observations. It was shown that this global

analysis error was high initially, especially in temperature and velocity. But as time progressed, the discrepancy between the assimilation and the true solution decreased because the model dynamics were able to propagate the assimilation corrections through the model domain. It is arguable that these errors would have decreased further to below a standard deviation, that is, the assimilation would eventually reproduce the true solution in the entire region had the system run long enough.

APPENDIX

Discretization of NCOM Equations

The discretization of NCOM uses second-order interpolation and differentiation as defined with the following notation:

$$\overline{\phi}^x = 0.5(\phi_{x+\Delta x/2} + \phi_{x-\Delta x/2}),$$

$$\left.\frac{\partial \phi}{\partial x}\right|_x = \frac{1}{\Delta x}\delta_x \phi = \frac{1}{\Delta x}(\phi_{x+\Delta x/2} - \phi_{x-\Delta x/2}),$$

and

$$\delta_{2t}\phi = (\phi_{t+\Delta t} - \phi_{t-\Delta t}).$$

The NCOM equations are then discretized in flux conservative form as follows

$$
\frac{\Delta x^u \Delta y^u}{2\Delta t}\delta_{2t}(\Delta z^u u) = \overline{\Delta x \Delta y \Delta z (f + C_{\text{curv}})\overline{v}^y}^x - \Delta y^u \Delta z^u g \delta_x(\zeta^* + \zeta_{\text{atm}} - \zeta_{\text{tp}}) - \Delta x^u \Delta z^u \frac{1}{\rho_0}\delta_x(p_i) - \delta_x(\overline{\Delta y^u \Delta z^u u^a}^x \overline{u}^x)
$$

$$
- \delta_y(\overline{\Delta x^v \Delta z^v v^a}^x \overline{u}^y) - \delta_z(\overline{\Delta x \Delta y w}\,\overline{u}^z) + \overline{\Delta x \Delta y \Delta z Q}^x u_{\text{sor}} + F_u^* + \Delta x^u \Delta y^u \delta_z\left[\frac{\overline{K_M}^x}{(\overline{\Delta z^{w^x}})^{n+1}}\delta_z u^{n+1}\right],
\tag{A1}
$$

$$
\frac{\Delta x^v \Delta y^v}{2\Delta t}\delta_{2t}(\Delta z^v v) = \overline{\Delta x \Delta y \Delta z (f + C_{\text{curv}})\overline{u}^x}^y - \Delta x^v \Delta z^v g \delta_y(\zeta^* + \zeta_{\text{atm}} - \zeta_{\text{tp}}) - \Delta x^v \Delta z^v \frac{1}{\rho_o}\delta_y(p_i) - \delta_x(\overline{\Delta y^u \Delta z^u u^a}^y \overline{v}^x)
$$

$$
- \delta_y(\overline{\Delta x^v \Delta z^v v^a}^x \overline{v}^y) - \delta_z(\overline{\Delta x \Delta y w}^y \overline{v}^z) + \overline{\Delta x \Delta y \Delta z Q}^y v_{\text{sor}} + F_v^* + \Delta x^v \Delta y^v \delta_z\left[\frac{\overline{K_M}^y}{(\overline{\Delta z^{w^y}})^{n+1}}\delta_z v^{n+1}\right],
\tag{A2}
$$

$$
\frac{\Delta x \Delta y}{2\Delta t}\delta_{2t}(\Delta z) - \delta_x(\Delta y^u \Delta z^u u^a) - \delta_y(\Delta x^v \Delta z^v v^a) - \delta_z(\Delta x \Delta y w),
\tag{A3}
$$

$$
\frac{\Delta x \Delta y}{2\Delta t}\delta_{2t}(\Delta z T) = -\delta_x(\Delta y^u \Delta z^u u^a \overline{T}^x) - \delta_y(\Delta x^v \Delta z^v v^a \overline{T}^y) - \delta_z(\Delta x \Delta y w \overline{T}^z) + \Delta x \Delta y \Delta z Q T_{\text{sor}}
$$

$$
+ \delta_x\left(\frac{\Delta y^u \Delta z^u A_H^u}{\Delta x^u}\delta_x T^{n-1}\right) + \delta_y\left(\frac{\Delta y^v \Delta z^v A_H^v}{\Delta y^v}\delta_y T^{n-1}\right) + \Delta x \Delta y \delta_z\left[\frac{K_H}{(\Delta z^w)^{n+1}}\delta_z T^{n+1}\right]
$$

$$
+ \Delta x \Delta y Q_r \delta_z \gamma \quad \text{and}
\tag{A4}
$$

$$
\frac{\Delta x \Delta y}{2\Delta t}\delta_{2t}(\Delta z S) = -\delta_x(\Delta y^u \Delta z^u u^a \overline{S}^x) - \delta_y(\Delta x^v \Delta z^v v^a \overline{S}^y) - \delta_z(\Delta x \Delta y w \overline{S}^z) + \Delta x \Delta y \Delta z Q S_{\text{sor}}
$$

$$
+ \delta_x\left(\frac{\Delta y^u \Delta z^u A_H^u}{\Delta x^u}\delta_x S^{n-1}\right) + \delta_y\left(\frac{\Delta y^v \Delta z^v A_H^v}{\Delta y^v}\delta_y S^{n-1}\right) + \Delta x \Delta y \delta_z\left[\frac{K_H}{(\Delta z^w)^{n+1}}\delta_z S^{n+1}\right].
\tag{A5}
$$

In (A1)–(A5), F_u and F_v are the horizontal mixing terms; ζ_{atm} and ζ_{tp} are the atmospheric surface pressure and tidal potential, respectively; and ζ^* is the surface elevation term that can be distributed among any of the three time levels, $\zeta^* = \alpha_1\zeta^{n+1} + \alpha_2\zeta^n + \alpha_3\zeta^{n-1}$, according to the temporal weighting terms α_1, α_2, or α_3, which are specified by the user. The horizontal mixing coefficients for the velocity and scalar fields (temperature and salinity) are A_M and A_H, respectively; likewise, K_M and K_M are used for the vertical mixing; Q is a volume flux source term (with T_{sor}, S_{sor}, u_{sor}, and v_{sor} as the term source values); Q_r is the solar radiation; γ is a function describing the solar extinction; Δx, Δy, and Δz denote the grid-cell dimensions defined at the center of the grid cells; and the superscripts u, v, and w indicate

the grid-cell dimensions computed at those velocity locations on the staggered Arakawa C grid. The Coriolis term is f; ρ_0 and p_i are the reference density of seawater and the internal pressure, respectively; and the horizontal advection velocity terms are given by u^a and v^a. The term C_{curv} is used to correct the horizontal advection of momentum for the horizontal curvature of the grid. It is calculated as

$$C_{curv} = \overline{v}^y\frac{\delta_{2x}(\Delta y)}{2\Delta x\Delta y} - \overline{u}^x\frac{\delta_{2y}(\Delta x)}{2\Delta x\Delta y}. \tag{A6}$$

The horizontal mixing terms for the momentum equations are given by

$$F_u^* = \delta_x\left[2\overline{\left(\frac{\Delta y^u\Delta z^u A_M^u}{\Delta x^u}\right)}^x\delta_x u^{n-1}\right] + \delta_y\left[\overline{\left(\frac{\Delta x^v\Delta z^v A_M^v}{\Delta y^v}\right)}^x\delta_y u^{n-1} + \overline{\left(\frac{\Delta x^v\Delta z^v A_M^v}{\Delta x^v}\right)}^x\delta_x v^{n-1}\right] \quad \text{and} \tag{A7}$$

$$F_v^* = \delta_x\left[\overline{\left(\frac{\Delta y^u\Delta z^u A_M^u}{\Delta y^u}\right)}^y\delta_y u^{n-1} + \overline{\left(\frac{\Delta y^u\Delta z^u A_M^u}{\Delta x^u}\right)}^y\delta_x v^{n-1}\right] + \delta_y\left[2\overline{\left(\frac{\Delta x^v\Delta z^v A_M^v}{\Delta y^v}\right)}^y\delta_y v^{n-1}\right], \tag{A8}$$

where the mixing coefficient is modeled according to Smagorinsky's formula:

$$A_M = C_{Smag}\Delta x\Delta y\left[\left(\frac{1}{\Delta x}\delta_x u^n\right)^2 + \frac{1}{2}\left(\frac{1}{2\Delta y}\delta_{2y}\overline{u^n}^x + \frac{1}{2\Delta x}\delta_{2x}\overline{v^n}^y\right)^2 + \left(\frac{1}{\Delta y}\delta_y v^n\right)^2\right]^{1/2}, \tag{A9}$$

with the magnitude of the eddy coefficient being scaled by the constant C_{Smag}. The vertical mixing coefficients are computed using the turbulence closure method of Mellor and Yamada in either its 2 or 2.5 version.

The computation for the free-surface mode is governed by the following equations:

$$\frac{\Delta x^u\Delta y^u}{2\Delta t}\delta_{2t}(D^u\overline{u}) = -\Delta y^u D^u g\delta_x(\alpha_1\zeta^{n+1} + \alpha_2\zeta^n + \alpha_3\zeta^{n-1}) + D^u\overline{G_u}, \tag{A10}$$

$$\frac{\Delta x^v\Delta y^v}{2\Delta t}\delta_{2t}(D^v\overline{v}) = -\Delta x^v D^v g\delta_y(\alpha_1\zeta^{n+1} + \alpha_2\zeta^n + \alpha_3\zeta^{n-1}) + D^v\overline{G_v}, \quad \text{and} \tag{A11}$$

$$\frac{\Delta x\Delta y}{2\Delta t}\delta_{2t}\zeta = -\delta_x\{\Delta y^u[\beta_1(\overline{D}^u u)^{n+1} + \beta_2(\overline{D}^u u)^n + \beta_3(\overline{D}^u u)^{n-1}]\} - \delta_y\{\Delta x^v[\beta_1(\overline{D}^v v)^{n+1} + \beta_2(\overline{D}^v v)^n + \beta_3(\overline{D}^v v)^{n-1}]\} + \Delta x\Delta y D\overline{Q}, \tag{A12}$$

where β_1, β_2, and β_3 are positive constants define by the user with $\beta_1 + \beta_2 + \beta_3 = 1$, and $D^u\overline{G_u}$ and $D^v\overline{G_v}$ are the vertical integrals of all the terms on the right-hand sides of (A1) and (A2), respectively, with the exception of the surface elevation gradient terms and the vertical mixing, and $D^u = \overline{D}^x$ and $D^v = \overline{D}^y$. The free-surface mode (A12) is solved by first substituting $(D^u\overline{u})^{n+1}$ and $(D^v\overline{v})^{n+1}$ into the time-discretized (A10) and (A11) into (A12), resulting in an elliptic equation that is solved for the surface elevation at time level $n + 1$, which is then substituted back into (A10) and (A11) to compute the barotropic transports $D^u\overline{u}$ and $D^v\overline{v}$, from which the barotropic velocities are obtained.

The vertical discretization uses a combination of sigma layers and z levels in a three-tiered distribution with (i) free sigma layers near the surface that expand and contract with the free surface elevation, (ii) fixed sigma layers that do not vary with the free surface, and (iii) fixed z levels that allow for partial bottom cells for a better match with the bottom topography.

REFERENCES

Amodei, L., 1995: Solution approchée pour un problème d'assimilation de données avec prise en compte de l'erreur du modèle. *C. R. Acad. Sci.,* **321,** 1087–1094.

Barron, C. N., R. C. Rhodes, L. F. Smedstad, C. D. Rowley, P. J. Martin, and A. B. Kara, 2003: Global ocean nowcasts and forecasts with the Navy Coastal Ocean Model (NCOM). *2003 NRL Review,* Naval Research Laboratory, 175–178.

——, A. B. Kara, H. E. Hurlburt, C. Rowley, and L. F. Smedstad, 2004: Sea surface height predictions from the global Navy Coastal Ocean Model (NCOM) during 1998–2001. *J. Atmos. Oceanic Technol.,* **21,** 1876–1894, doi:10.1175/JTECH-1680.1.

——, ——, P. J. Martin, R. C. Rhodes, and L. F. Smedstad, 2006: Formulation, implementation and examination of vertical coordinate choices in the Global Navy Coastal Ocean Model (NCOM). *Ocean Modell.,* **11,** 347–375, doi:10.1016/j.ocemod.2005.01.004.

Bennett, A. F., 1992: *Inverse Methods in Physical Oceanography.* Cambridge University Press, 347 pp.

——, 2002: *Inverse Modeling of the Ocean and Atmosphere.* Cambridge University Press, 260 pp.

——, B. S. Chua, and L. M. Leslie, 1996: Generalized inversion of a global numerical weather prediction model. *Meteor. Atmos. Phys.,* **60,** 165–178, doi:10.1007/BF01029793.

Book, J. W., P. J. Martin, I. Janekovic, M. Kuzmic, and M. Wimbush, 2009: Vertical structure of bottom Ekman tidal flows: Observations, theory, and modeling from the northern Adriatic. *J. Geophys. Res.,* **114,** C01S06, doi:10.1029/2008JC004736.

Broquet, G., C. A. Edwards, A. M. Moore, B. S. Powell, M. Veneziani, and J. D. Doyle, 2009: Application of 4D-variational data assimilation to the California Current System. *Dyn. Atmos. Oceans,* **48,** 69–92, doi:10.1016/j.dynatmoce.2009.03.001.

——, A. M. Moore, H. G. Arango, and C. A. Edwards, 2011: Corrections to ocean surface forcing in the California Current System using 4D variational data assimilation. *Ocean Modell.,* **36,** 116–132, doi:10.1016/j.ocemod.2010.10.005.

Brushett, B. A., B. A. King, and C. J. Lemckert, 2011: Evaluation of met-ocean forecast data effectiveness for tracking drifters deployed during operational oil spill response in Australian waters. *J. Coastal Res.,* **64,** 991–994.

Burrage, D. M., J. W. Book, and P. J. Martin, 2009: Eddies and filaments of the western Adriatic Current near Cape Gargano: Analysis and prediction. *J. Mar. Syst.,* **78,** S205–S226, doi:10.1016/j.jmarsys.2009.01.024.

Chao, Y., and Coauthors, 2009: Development, implementation and evaluation of a data-assimilative ocean forecasting system off the central California coast. *Deep-Sea Res. II,* **56,** 100–126, doi:10.1016/j.dsr2.2008.08.011.

Cheng, Y. C., X. F. Li, Q. Xu, O. Garcia-Pineda, O. B. Andersen, and W. G. Pichel, 2011: SAR observation and model tracking of an oil spill event in coastal waters. *Mar. Pollut. Bull.,* **62,** 350–363, doi:10.1016/j.marpolbul.2010.10.005.

Chua, B. S., and A. F. Bennett, 2001: An inverse ocean modeling system. *Ocean Modell.,* **3,** 137–165, doi:10.1016/S1463-5003(01)00006-3.

Daley, R., 1992: *Atmospheric Data Analysis.* Cambridge University Press, 472 pp.

Derber, J., and A. Rosati, 1989: A global oceanic data assimilation system. *J. Phys. Oceanogr.,* **19,** 1333–1347, doi:10.1175/1520-0485(1989)019<1333:AGODAS>2.0.CO;2.

Di Lorenzo, E., A. Moore, H. Arango, Chua, B. D. Cornuelle, A. J. Miller, B. Powell, and A. Bennett, 2007: Weak and strong constraint data assimilation in the inverse Regional Ocean Modeling System (ROMS): Development and application for a baroclinic coastal upwelling system. *Ocean Modell.,* **16,** 160–187, doi:10.1016/j.ocemod.2006.08.002.

Egbert, G. D., A. F. Bennett, and M. G. G. Foreman, 1994: TOPEX/POSEIDON tides estimated using a global inverse method. *J. Geophys. Res.,* **99,** 24 821–24 852, doi:10.1029/94JC01894.

Erwig, M., Z. Fu, and B. Pflaum, 2007: Parametric Fortran: Program generation in scientific computing. *J. Software Maint. Evol.,* **19,** 155–182, doi:10.1002/smr.346.

Goerss, J. S., and P. A. Phoebus, 1992: The Navy's operational atmospheric analysis. *Wea. Forecasting,* **7,** 232–249, doi:10.1175/1520-0434(1992)007<0232:TNOAA>2.0.CO;2.

Haley, P. J., and Coauthors, 2009: Forecasting and reanalysis in the Monterey Bay/California Current region for the Autonomous Ocean Sampling Network-II experiment. *Deep-Sea Res. II,* **56,** 127–148, doi:10.1016/j.dsr2.2008.08.010.

Haza, A. C., L. I. Piterbarg, P. Martin, T. M. Ozgokmen, and A. Griffa, 2007: A Lagrangian subgridscale model for particle transport improvement and application in the Adriatic Sea using the Navy Coastal Ocean Model. *Ocean Modell.,* **17,** 68–91, doi:10.1016/j.ocemod.2006.10.004.

Hodur, R. M., 1997: The Naval Research Laboratory's Coupled Ocean/Atmosphere Mesoscale Prediction System (COAMPS). *Mon. Wea. Rev.,* **125,** 1414–1430, doi:10.1175/1520-0493(1997)125<1414:TNRLSC>2.0.CO;2.

Jacobs, G. A., and H. E. Ngodock, 2003: The maintenance of conservative physical laws within data assimilation systems. *Mon. Wea. Rev.,* **131,** 2595–2607, doi:10.1175/1520-0493(2003)131<2595:TMOCPL>2.0.CO;2.

Jolliff, J. K., J. C. Kindle, I. Shulman, B. Penta, M. A. M. Friedrichs, R. Helber, and R. A. Arnone, 2009: Summary diagrams for coupled hydrodynamic-ecosystem model skill assessment. *J. Mar. Syst.,* **76,** 64–82, doi:10.1016/j.jmarsys.2008.05.014.

Kara, A. B., C. N. Barron, P. J. Martin, L. F. Smedstad, and R. C. Rhodes, 2006: Validation of interannual simulations from the 1/8 degree global Navy Coastal Ocean Model (NCOM). *Ocean Modell.,* **11,** 376–398, doi:10.1016/j.ocemod.2005.01.003.

Liu, Y. G., P. MacCready, B. M. Hickey, E. P. Dever, P. M. Kosro, and N. S. Banas, 2009: Evaluation of a coastal ocean circulation model for the Columbia River plume in summer 2004. *J. Geophys. Res.,* **114,** C00B04, doi:10.1029/2008JC004929.

Marotzke, J., R. Giering, K. Q. Zhang, D. Stammer, C. Hill, and T. Lee, 1999: Construction of the adjoint MIT ocean general circulation model and application to Atlantic heat transport sensitivity. *J. Geophys. Res.,* **104,** 29 529–29 547, doi:10.1029/1999JC900236.

Martin P., 2000: Description of the Navy Coastal Ocean Model Version 1.0. NRL Rep. NRL/FR/7322—00-9962, 45 pp. [Available online at http://oai.dtic.mil/oai/oai?verb=getRecord&metadataPrefix=html&identifier=ADA387444.]

Moore, A. M., H. G. Arango, E. Di Lorenzo, B. D. Cornuelle, A. J. Miller, and D. J. Neilson, 2004: A comprehensive ocean prediction and analysis system based on the tangent linear and adjoint of a regional ocean model. *Ocean Modell.,* **7,** 227–258, doi:10.1016/j.ocemod.2003.11.001.

Morey, S. L., P. J. Martin, J. J. O'Brien, A. A. Wallcraft, and J. Zavala-Hidalgo, 2003: Export pathways for river discharged fresh water in the northern Gulf of Mexico. *J. Geophys. Res.,* **108,** 3303, doi:10.1029/2002JC001674.

Ngodock, H. E., 2005: Efficient implementation of covariance multiplication for data assimilation with the representer method. *Ocean Modell.,* **8,** 237–251, doi:10.1016/j.ocemod.2003.12.005.

——, and M. J. Carrier, 2013: A weak constraint 4D-Var assimilation system for the Navy Coastal Ocean Model using the representer method. *Data Assimilation for Atmospheric, Oceanic and Hydrologic Applications,* Vol. II, S. K. Park and L. Xu, Eds., Springer-Verlag, doi:10.1007/978-3-642-35088-7_15.

——, and ——, 2014: A 4DVAR system for the Navy Coastal Ocean Model. Part II: Strong and weak constraint assimilation experiments with real observations in Monterey Bay. *Mon. Wea. Rev.,* **142,** 2108–2117, doi:10.1175/MWR-D-13-00220.1.

——, B. S. Chua, and A. F. Bennett, 2000: Generalized inversion of a reduced gravity primitive equation ocean model and tropical atmosphere ocean data. *Mon. Wea. Rev.,* **128,** 1757–1777, doi:10.1175/1520-0493(2000)128<1757:GIOARG>2.0.CO;2.

——, S. R. Smith, and G. A. Jacobs, 2007: Cycling the representer algorithm for variational data assimilation with the Lorenz attractor. *Mon. Wea. Rev.,* **135,** 373–386, doi:10.1175/MWR3281.1.

——, ——, and ——, 2009: Cycling the representer method with nonlinear models. *Data Assimilation for Atmospheric, Oceanic and Hydrologic Applications,* S. K. Park and L. Xu, Eds., Springer, 321–340, doi:10.1007/978-3-540-71056-1_17.

Pullen, J., J. D. Doyle, and R. P. Signell, 2006: Two-way air–sea coupling: A study of the Adriatic. *Mon. Wea. Rev.,* **134,** 1465–1483, doi:10.1175/MWR3137.1.

——, ——, T. Haack, C. Dorman, R. P. Signell, and C. M. Lee, 2007: Bora event variability and the role of air-sea feedback. *J. Geophys. Res.,* **112,** C03S18, doi:10.1029/2006JC003726.

Rosmond, T. E., 1992: The design and testing of the Navy Operational Global Atmospheric Prediction System. *Wea. Forecasting,* **7,** 262–262, doi:10.1175/1520-0434(1992)007<0262:TDATOT>2.0.CO;2.

Schroeder, K., A. C. Haza, A. Griffa, T. M. Ozgokmen, P. M. Poulain, R. Gerin, G. Peggion, and M. Rixen, 2011: Relative dispersion in the Liguro-Provencal basin: From sub-mesoscale to mesoscale. *Deep-Sea Res. I,* **58,** 209–228, doi:10.1016/j.dsr.2010.11.004.

Shulman, I., C. R. Wu, J. K. Lewis, J. D. Paduan, L. K. Rosenfeld, J. C. Kindle, S. R. Ramp, and C. A. Collins, 2002: High resolution modeling and data assimilation in The Monterey Bay. *Cont. Shelf Res.,* **22,** 1129–1151, doi:10.1016/S0278-4343(01)00100-5.

——, and Coauthors, 2007: Modeling of upwelling/relaxation events with the Navy Coastal Ocean Model. *J. Geophys. Res.,* **112,** C06023, doi:10.1029/2006JC003946.

——, and Coauthors, 2009: Impact of glider data assimilation on the Monterey Bay Model. *Deep-Sea Res.,* **56,** 188–198, doi:10.1016/j.dsr.2008.08.003.

——, M. A. Moline, B. Penta, S. Anderson, M. Oliver, and S. H. D. Haddock, 2011: Observed and modeled bio-optical, bio-luminescent, and physical properties during a coastal upwelling event in Monterey Bay, California. *J. Geophys. Res.,* **116,** C01018, doi:10.1029/2010JC006525.

Stammer, D., and Coauthors, 2002: The global ocean circulation during 1992–1997, estimated from ocean observations and a general circulation model. *J. Geophys. Res.,* **107,** 3118, doi:10.1029/2001JC000888.

Talagrand, O., 1999: A posteriori evaluation and verification of analysis and assimilation algorithms. *Proc. Workshop on Diagnosis of Data Assimilation Systems,* Reading, United Kingdom, ECMWF, 17–28.

Weaver, A., and P. Courtier, 2001: Correlation modeling on the sphere using a generalized diffusion equation. *Quart. J. Roy. Meteor. Soc.,* **127,** 1815–1846, doi:10.1002/qj.49712757518.

——, J. Vialard, and D. L. T. Anderson, 2003: Three- and four-dimensional variational assimilation with a general circulation model of the tropical Pacific Ocean. Part I: Formulation, internal diagnostics, and consistency checks. *Mon. Wea. Rev.,* **131,** 1360–1378, doi:10.1175/1520-0493(2003)131<1360:TAFVAW>2.0.CO;2.

Wunsch, C., 2006: *Discrete Inverse and State Estimation Problems: With Geophysical Fluid Applications.* Cambridge University Press, 371 pp.